Time-Lapse Acoustic Imaging of Mesoscale and Fine-Scale Variability within the Faroe-Shetland Channel

Alex Dickinson[1*], **N. J. White**[1], **C. P. Caulfield**[2,3]

[1]Bullard Laboratories, Department of Earth Sciences, University of Cambridge, Cambridge, UK

[2]BP Institute, University of Cambridge, Cambridge, UK

[3]Department of Applied Mathematics and Theoretical Physics, University of Cambridge, Cambridge, UK

Key Points:

- Time-lapse acoustic imaging of thermohaline structure over 25 days
- Spatial and temporal deflection of pycnocline caused by rapidly moving vortex
- Acoustic imaging resolves cascade of energy from mesoscale to turbulent motions

[*]Department of Physics, University of York, York, UK

Corresponding author: , nad38@alumni.cam.ac.uk, njw10@cam.ac.uk

This article has been accepted for publication and undergone full peer review but has not been through the copyediting, typesetting, pagination and proofreading process which may lead to differences between this version and the Version of Record. Please cite this article as doi: 10.1029/2019JC015861

©2020 American Geophysical Union. All rights reserved.

Abstract

We describe and analyze the results of a three-dimensional seismic (i.e. acoustic) reflection survey from the Faroe-Shetland Channel that is calibrated with near-coincident hydrographic and satellite observations. 54 vertical seismic transects were acquired over a period of 25 days. On each transect, a 250–400 m band of reflections is observed within the water column. Hydrographic measurements demonstrate that this reflective band is caused by temperature variations within the pycnocline that separates warm, near-surface waters of Atlantic origin from cold, deep waters which flow southward from the Nordic Seas. Tilting of reflective surfaces records geostrophic shear between these near-surface and deep waters. Measurements of temporal changes of pycnoclinic depth and of reflection tilt are used to infer the existence of an anticyclonic vortex that advects northeastward. Comparison with satellite measurements of sea-surface temperature and height suggests that this vortex is caused by meandering of the Continental Slope Current. A model of a Gaussian vortex is used to match seismic and satellite observations. This putative vortex has a core radius of 20–30 km and a maximum azimuthal velocity of 0.3–0.4 m s^{-1}. It translates at 0.01–0.1 m s^{-1}. Within the pycnocline, diapycnal diffusivity, K, is estimated by analyzing the turbulent spectral subrange of tracked reflections. K varies between $10^{-5.7}$ and $10^{-5.0}$ m^2 s^{-1} in a pattern that is broadly consistent with translation of the vortex. Our integrated study demonstrates the ability of time-lapse seismic reflection surveying to dynamically resolve the effects that mesoscale activity has upon deep thermohaline structure on scales from meters to hundreds of kilometers.

1 Introduction

The global overturning circulation is driven by a cascade of energy across scales ranging from millimeters to thousands of kilometers (Ferrari & Wunsch, 2009). This cascade involves interactions between geostrophically balanced motions, internal waves, and small-scale turbulence (Wunsch & Ferrari, 2004). Over the last century, development of specialised instrumentation such as conductivity-temperature-depth (CTD) probes, shear probes and observational satellites has revolutionized our understanding of this cascade (e.g. Apel, 1972; Gregg & Cox, 1971; Jacobsen, 1948). However, it has proven difficult to simultaneously acquire measurements on all relevant scales (Ferrari, 2014; Ferrari & Wunsch, 2010). Development of an improved understanding using new observational tech-

©2020 American Geophysical Union. All rights reserved.

niques will be the key to accurately parametrizing the overturning circulation and assessing its effect on climate (McWilliams, 2016).

Seismic (i.e., acoustic) imaging provides an important new tool with which to investigate the energy cascade. Variations of temperature and salinity within the water column cause changes in acoustic impedance, which is the product of sound speed and density, that are observable using standard seismic reflection profiling (Holbrook, Páramo, Pearse, & Schmitt, 2003). This profiling can image the structure of the water column down to abyssal depths over ranges of hundreds of kilometers and it is sensitive to temperature contrasts as small as 0.03°C (Nandi, Holbrook, Pearse, Páramo, & Schmitt, 2004). Significantly, seismic images have vertical and horizontal resolutions on the order of 10 m. Equal resolution in both vertical and horizontal directions distinguishes this imagery from conventional sampling methods (e.g. acquisition of hydrographic casts along a transect). The combination of long-range transects and high resolution makes seismic imaging ideally suited for exploring dynamical links between mesoscale motion on horizontal length scales of up to $\sim O(10^5)$ m and turbulence on horizontal length scales of $\sim O(10^2)$ m (B. R. Ruddick, 2018).

Previous seismic reflection studies of thermohaline structure have mostly been limited to analysis of individual transects, referred to here as two-dimensional seismic surveys. Three-dimensional seismic surveys are designed so that tens to hundreds of closely spaced transects are acquired within a small area over short periods of days to weeks. These sets of transects enable the evolution of fine-scale structure to be determined through time and space. Blacic and Holbrook (2010) have observed internal waves on a three-dimensional survey that was acquired over the course of a single day. Tang, Tong, Hobbs, and Maqueda (2019) have monitored the evolution of an individual thermohaline layer using three closely spaced seismic transects that were acquired over a period of four days. Notwithstanding these studies, the potential of three-dimensional surveys to repeatedly image localized thermohaline structures over a period of several weeks, which was first recognized by Pearse, Holbrook, Paramo, and Schmitt (2003), has not yet been fully exploited. Here, we show how this time-lapse imaging is uniquely capable of probing large volumes of water mass with a view to understanding spatial and temporal variations of mesoscale and fine-scale structures from the sea surface to the sea bed.

©2020 American Geophysical Union. All rights reserved.

We exploit seismic reflection records acquired over a period of 25 days in summer 1997 to investigate the energy cascade within the Faroe-Shetland Channel. This channel is an important conduit for northward transport of heat and salt from the Atlantic Ocean to the Nordic Seas, and for southward flow of cold deep waters that form a significant component of the Meridional Overturning Circulation (e.g., Berx et al., 2013; Olsen, Hansen, Quadfasel, & Østerhus, 2008; Østerhus et al., 2019). However, quantification of mean fluxes through the channel is complicated by intense activity at the mesoscale and at fine scales. Developing an understanding of the effects of this activity, which includes eddies, trains of solitary waves, and an internal tide with an amplitude of ~ 40 m, is essential to accurately parametrizing climatic models (e.g. H. Dooley, 1975; H. D. Dooley & Meincke, 1981; Hall, Berx, & Damerell, 2019; Hall, Huthnance, & Williams, 2011; Hosegood, Bonnin, & van Haren, 2004; T. Sherwin, 1991; T. J. Sherwin, Turrell, Jeans, & Dye, 1999; T. J. Sherwin, Williams, Turrell, Hughes, & Miller, 2006). Mesoscale and fine-scale fluctuations within the channel have important implications for fish stocks and for the safe operation of deep-sea rigs (e.g., Gallego et al., 2018; Hansen & Jákupsstovu, 1992; Shelton, Turrell, Macdonald, McLaren, & Nicoll, 1997).

Our investigation is divided into a series of steps. First, we summarize the regional hydrography and gauge its response to seismic imaging. Secondly, a three-dimensional seismic survey is processed using an adapted methodology to yield 54 time-lapse acoustic images that reveal the thermohaline structure within part of the channel. Thirdly, we develop methods for estimating interface depths, current flow, and diapycnal diffusivities from these spectacular images. Fourthly, the temporal variation of interface depths and of current flow are accounted for using a simplified dynamical model. This model is tested against coincident satellite measurements of sea-surface temperature and of sea-surface height. Finally, the physical implications of our results for northward flux of heat and salt are discussed.

2 Hydrographic Framework

We outline the hydrography of the Faroe-Shetland Channel, paying particular attention to the way in which thermohaline structure is acoustically recorded by seismic profiling. Seismic reflection experiments typically exploit acoustic waves within a frequency range of 15–45 Hz. At these frequencies, vertically propagating acoustic waves are sensitive to temperature and salinity changes on vertical length scales of $\lesssim 100$ m.

©2020 American Geophysical Union. All rights reserved.

Accepted Article

Local hydrography is illustrated using 26 CTD casts that were acquired in the deep (i.e., > 800 m) portion of the channel during June-September 1997 (Figures 1b and 2a,b). Composition of waters within the upper $\sim$ 300–600 m above the Shetland slope is predominantly determined by the Continental Slope Current, which transports warm saline North Atlantic Water (NAW) northeastward into the Nordic Seas (Figure 1a; Booth & Ellett, 1983; Swallow, Gould, & Saunders, 1977). Waters within the upper $\sim$ 300–600 m of the deep channel are mainly composed of Modified North Atlantic Water (MNAW; Hansen & Østerhus, 2000). Conservative temperature, Θ, and absolute salinity, S_A, vary slowly as a function of depth within these upper layers with minor fluctuations of ~ 0.1°C and ~ 0.02 g kg^{-1} on vertical length scales of ~ 10 m. These fluctuations are expected to give rise to weak seismic reflections. Within the deeper part of the channel, a pycnocline at 300–700 m separates NAW and MNAW from deep overflow waters (e.g., Gould, Loynes, & Backhaus, 1985; Larsen, Hansen, Kristiansen, & Østerhus, 2000). Within this pycnocline, Θ and S_A decrease rapidly as a function of depth ($0°\text{C} \lesssim \Theta \lesssim 7°\text{C}$ and $35.1 \text{ g kg}^{-1} \lesssim S_A \lesssim 35.4 \text{ g kg}^{-1}$). Fluctuations on the order of 1°C and 0.05 g kg^{-1} over vertical length scales of order 10 m are expected to give rise to clearly visible seismic reflections. Cold overflow waters are found at depths greater than 500–700 m. These waters are dominated by Norwegian Sea Deep Water (NSDW) with smaller quantities of Norwegian Sea Arctic Intermediate Water (NSAIW) and Modified East Icelandic Water (MEIW) at intermediate depths (Hansen & Østerhus, 2000). Θ and S_A have nearly constant values of -1 °C and 35.1 g kg^{-1}, respectively. Thus sharp contrasts on seismically resolvable vertical length scales are not observed.

The response of thermohaline structure to transmission and reflection of acoustic waves can be quantitatively investigated by constructing synthetic seismograms. Profiles of *in situ* density and bulk modulus are first calculated using the GSW TEOS-10 empirical equation of state for seawater (IOC, SCOR, & IAPSO, 2010). Vertical propagation of a Ricker wavelet with a peak frequency of 30 Hz through these profiles is numerically simulated by using a one-dimensional spectral element method (Komatitsch & Tromp, 1999; Wang, 2015). This method is a suitable first-order approximation that includes multiple internal reflections but does not account for non-normal incidence of waves or for repeated signal sampling. In order to enable comparison with observed seismic images, two-way travel time is converted into depth by assuming a constant sound speed of 1480 m s^{-1}, frequency content is filtered using a low-cut (< 30 Hz) Butterworth frequency filter, and

©2020 American Geophysical Union. All rights reserved.

reflections within the top 100 m are excised. Resultant synthetic seismograms show that bands of bright reflectivity match observed temperature and salinity changes within the pycnocline (e.g. Figure 2i). Above and below the pycnocline, reflectivity is either weak or absent.

In order to dynamically interpret these bright reflections, it is important to understand how they relate to isothermal and isopycnal surfaces within the pycnocline. We compute *in situ* density, ρ, potential density, ρ_θ, buoyancy frequency, N, sound speed, c, and acoustic impedance, I, from CTD profiles using the GSW TEOS-10 equation of state (IOC et al., 2010). Profiles of N are smoothed using a boxcar filter of length 100 m to eliminate regions of unstable stratification (Figure 2c). Comparison with profiles of N that were computed using decimated depth intervals suggests that smoothed profiles are sensitive to changes in density over vertical distances of $\gtrsim 10$ m. Θ, c and I are strongly correlated with each other within the pycnocline (i.e. $r \approx 0.99$), suggesting that reflectivity is predominantly controlled by temperature rather than by salinity (Figure 2a,g,h; B. Ruddick, Song, Dong, & Pinheiro, 2009). Following Sallarès et al. (2009), we estimate that temperature variations are responsible for $\sim 95\%$ of observed reflectivity. Seismic reflections therefore closely track isothermal surfaces within the pycnocline. Observational studies and numerical simulations suggest that correspondence between reflective and isopycnal surfaces depends upon local hydrography (e.g. Barbosa Aguiar, Ménesguen, Le Gentil, Schopp, & Carton, 2015; Biescas et al., 2014; Holbrook et al., 2013; Krahmann, Papenberg, Brandt, & Vogt, 2009; Meunier et al., 2019). A rigorous determination of the local relationship between reflective and isopycnal surfaces is beyond the scope of this study. However, following the approach of Sheen, White, Caulfield, and Hobbs (2011), we note that there is a reasonable correspondence between vertical profiles of $(\partial\rho_\theta/\partial z)$ and of reflection coefficients, R, computed directly from CTD casts. In particular, extremal values of $(\partial\rho_\theta/\partial z)$ correspond to extremal values of R, suggesting that the brightest reflections track isopycnal surfaces.

3 Seismic Reflection Images

3.1 Survey Acquisition

A three-dimensional seismic survey was acquired close to the center of the Faroe-Shetland Channel by the vessel PGS Ramform Explorer between 27 July and 20 August

©2020 American Geophysical Union. All rights reserved.

Accepted Article

1997 (Figure 1b). Acquisition dates are referred to by Year Day so that 27 July = Day 208 and 20 August = Day 232. During acquisition, the vessel repeatedly traversed the axis of the channel, alternating between travelling from southwest to northeast and from northeast to southwest in what is referred to as racetrack mode. This form of acquisition is carried out to enable broad turning which is necessary when these seismic surveys are carried out. In this way, the vessel acquired 54 parallel transects that can be divided into two groups, labeled Sector A and Sector B (Figure 1c). The 27 transects of each sector were acquired while the vessel travelled northeastward (A) or southwestward (B). Note that transect B27 is anomalous since it was acquired in a northeastward direction. Sectors A and B are located to the northwest and to the southeast, respectively (Figure 1c). Each transect is labeled according to its position within the sector. Thus transects A1 and A27 are the first and last transects to have been acquired within Sector A (Figure 1b). Sequential acquisition by racetrack mode means that adjacent transects within the same sector (e.g. A1 and A2) are spatially separated by ~ 300 m in the cross-channel (i.e. northwest-southeast) direction but temporally separated by ~ 1 day. Subsequent transects from different sectors (e.g. A1 and B1) are spatially separated by $\sim$ 9 km in the cross-channel direction and temporally separated by $\sim$ 12 hours. The 27 transects of Sector A are ~ 9 km long and are located in water depths of 1070–1100 m. The 27 transects of Sector B are ~ 7 km long and are located in water depths of 970–1070 m.

Vessel speed, u_v, varied between ~ 1.8 m s^{-1} and ~ 2.5 m s^{-1} (Table A.1). Mean values of u_v for Sector A and Sector B are 2.29 ± 0.15 m s^{-1} and 2.08 ± 0.15 m s^{-1}, respectively. Average speed for Sector B is probably lower because the vessel was travelling against the strong northeastward-flowing Continental Slope Current (Booth & Ellett, 1983; Swallow et al., 1977). Sea-surface conditions were generally good during seismic surveying, although acquisition was briefly halted on Day 211 and on Day 212 due to strong surface waves. See Table A.1 for further acquisition details.

The seismic vessel towed two acoustic sources at an average depth of 7.5 m that were separated by 50 m in the cross-streamer (i.e. northwest-southeast) direction. Each of these sources comprised a tuned array of airguns with a total volume 3090 cubic inches, which was primed with air that had a pressure of 2000 psi. The two sources were alternately fired every 10–14 s depending upon the speed of the vessel, which corresponds to a distance along the ground of 25 m. Each source generated an acoustic impulse (i.e. source

©2020 American Geophysical Union. All rights reserved.

wavelet) that closely approximates a Ricker wavelet with a peak frequency of 15–45 Hz (Wang, 2015). This impulse was principally directed downward through the water column where it was progressively transmitted and reflected at boundaries where acoustic impedance changed. Reflected waves were recorded along eight streamers (i.e. cables of hydrophones), which were each 3.6 km long and towed at an average depth of 9 m. The nominal (i.e. intended) lateral separation between adjacent streamers was 50 m and each streamer had 288 hydrophone arrays that were spaced every 12.5 m. The hydrophone sampling interval was 2 ms. Under optimal conditions, each transect consists of 16 nominal lines that are separated laterally by 25 m. Each of these lines has a nominal fold of cover (i.e. redundancy) of 36. Comprehensive accounts of seismic acquisition procedure and terminology are given by Sheriff and Geldart (1995), B. Ruddick et al. (2009) and Song, Pinheiro, Ruddick, and Huang (2012).

3.2 Signal Processing

Processing of seismic reflection data has been carried out using standard methods that are adapted from those used to construct images of the solid Earth (Yilmaz, 2001). There are three important steps. First, noise is removed from the records. Ambient noise generated by surface waves and by mechanical vibration is suppressed using a low-cut (< 30 Hz) Butterworth frequency filter. After filtering, reflections from the solid Earth are excised. Sound that propagates directly from the source toward the receivers is removed using an adaptive filter. Seismic amplitudes are approximately corrected to account for geometric spreading of the wave field as it propagates through the water column.

Secondly, recorded positions of source and receivers for each airgun shot are used to calculate the midpoint coordinates of each source-receiver pair. Based on these coordinates, records are binned into a two-dimensional spatial grid. Cells within this grid are referred to as common midpoints (cmps). Data from different source-receiver pairs are recorded many times at each cmp, enhancing the signal-to-noise ratio. Under optimal conditions, data acquired by this seismic survey should be binned using a cmp grid with a spacing 6.25 m parallel to direction of travel and 25 m perpendicular to this direction. During surveying, however, the streamers were laterally deflected from their intended positions by strong surface currents. This deflection reduced the number of times that each cmp location was sampled, which degrades the signal-to-noise ratio. We found

©2020 American Geophysical Union. All rights reserved.

that the best compromise between spatial resolution and signal-to-noise ratio was achieved by binning data using a cmp grid with a spacing 6.25 m parallel to direction of travel and 50 m perpendicular to this direction.

Thirdly, seismic records belonging to the same cmp are added together to generate coherent seismic signals with improved signal-to-noise ratios. This procedure is known as stacking. Sesimic data are recorded as a function of the time that elapses between generation and detection of acoustic energy, which is referred to as two-way travel time. Horizontal separation between source and receivers leads to a progressive time delay called normal move-out. Before stacking, records must be corrected for this normal move-out. Accurate correction is predicated upon knowledge of the root-mean-square (rms) sound speed of seawater as a function of two-way travel time. The rms sound speed can be extracted directly from seismic data by analyzing source-receiver pairs that belong to the same cmp. A profile of sound speed as a function of two-way travel time is selected that maximizes the coherency between seismic reflections recorded at different source-receiver separations. This procedure is known as velocity analysis. Velocity analysis for the water column is generally carried out by hand. Fortunately, this particular seismic survey has an excellent signal-to-noise ratio and we found that an automated velocity analysis algorithm performed well. Velocity analysis was carried out every 312.5 m in the along-streamer direction and every 50 m in the cross-streamer direction. Excessive frequency distortion at large source-receiver separation is minimized by applying a stretch mute of 0.5 (Buchholtz, 1972; Yilmaz, 2001). Seismic records were not spatially migrated since migration algorithms can significantly damage spectral content at high horizontal wavenumbers (Dickinson, White, & Caulfield, 2017; Falder, White, & Caulfield, 2016).

Following normal move-out correction, cmp records are stacked together which improves the signal-to-noise ratio. 36 source-receiver pairs belong to each cmp. These pairs were acquired during a time interval of between 12 and 17 minutes (Falder et al., 2016). Application of the stretch mute excises records that take the longest duration to record. On each image, information contributing to a single point on a reflection at a depth of 700 m is therefore recorded over an interval of 5–7 minutes, depending upon vessel speed. A single point on a shallower reflection is imaged over a shorter interval of time. Note that an interval of < 7 minutes is much shorter than the mean buoyancy period within the pycnocline ($N \lesssim 3$ cph; Figure 2). We are therefore confident that individual points along a given reflection can be regarded as being close to stationary. It is important to

©2020 American Geophysical Union. All rights reserved.

emphasize that this conclusion applies only to individual points on an image. All of the information on a single image that is ~ 9 km long is recorded over a period of 60–80 minutes during which thermohaline structure will evolve. Note that thermohaline structure will significantly change over the 25 days taken to acquire all 54 transects.

Signal processing yields a suite of 54 transects, each of which consists of up to nine parallel seismic images that are $\lesssim 9$ km long and separated by 50 m. Each image can be regarded as a vertical slice through the water column extending from the sea surface to the sea bed. Here, we do not exploit the three-dimensional nature of parallel images belonging to a single transect. Instead, we select one image from the center of each transect and analyse time-lapse variations between different transects.

3.3 Reflective Structure

Most of the 54 seismic images are characterized by a band of bright reflections that corresponds to the deep pycnocline (Figures 3 and 4). Reflections within the pycnocline are generally continuous over several kilometers and sometimes span the entire length of an image ($\lesssim 9$ km). Undulations with wavelengths $\sim$ 1–2 km and amplitudes $\lesssim 30$ m are indicative of an energetic internal wave field (e.g. Figure 3i). Many, but not all, of these undulations have narrow peaks, which suggests that they are non-linear internal solitary waves similar to those observed by Hosegood et al. (2004) and by Hall et al. (2011). At greater depths, reflectivity is absent due to the homogeneity of FSCBW. Above the pycnocline, several images have shorter and fainter reflections. For example, a near-surface band of reflections at depths shallower than ~ 200 m is visible on many images. This band probably corresponds to a seasonal near-surface pycnocline that typically develops during June-October (e.g., Turrell, Hansen, Hughes, & Østerhus, 2003).

Note that it is not straightforward to identify specific water masses on these seismic images. We henceforth refer to all water masses above the pycnocline (i.e. NAW and MNAW) as Faroe-Shetland Channel Upper Water (FSCUW). Water masses below the pycnocline (i.e. NSDW, NSAIW and MEIW) are referred to as Faroe-Shetland Channel Bottom Water (FSCBW; Turrell, Slesser, Adams, Payne, & Gillibrand, 1999). E. A. Vsemirnova, Hobbs, and Hosegood (2012) observe the deep pycnocline on a similar seismic image within the Faroe-Shetland Channel. However, they do not analyze the pycnoclinic fine-scale struc-

©2020 American Geophysical Union. All rights reserved.

ture in detail. Instead, they focus on analysis of turbid layers within the lowermost ∼ 100 m of the water column.

Taken together, our 54 seismic images reveal three striking features (Figure 4). First, the depth of the seismically imaged pycnocline clearly varies by ∼ 400 m across the suite of images. Secondly, reflections within the pycnocline are often steeply tilted with respect to the horizontal. Thirdly, it is notable that images from Sectors A and B have closely similar variations of pycnoclinic depth and of reflection tilt. It is likely that these variations are caused by a temporally varying phenomenon and not by the spatial separation between different transects. We investigate this variation by developing quantitative methods for mapping changes in pycnoclinic depth, in reflection tilt, and in turbulent mixing.

4 Properties of Seismically Imaged Pycnocline

4.1 Depth Measurements

Upper and lower boundaries of the seismically imaged pycnocline are identified on each image using an objective method that is based upon changes of seismic amplitude as a function of depth. The uppermost 150 m and the outermost 1 km on each side of an image are excluded to avoid contamination resulting from the presence of bright near-surface reflections and from low fold of cover, respectively. First, stacked seismic amplitudes are converted into absolute values by replacing negative amplitudes with their moduli (Figure 5b). Secondly, these absolute values are vertically smoothed using a boxcar filter of length 32 samples (∼ 50 m; Figure 5c). Thirdly, smoothed values are horizontally averaged to yield a single profile, which represents variation in mean amplitude as a function of depth (i.e. Profile D; Figure 5d). Fourthly, Profile D is normalized in order to identify rapid changes of amplitude with depth. To identify the upper boundary of the band of bright reflections, the value of Profile D at any depth is normalized by the mean value of the profile at all shallower depths to give Profile E (Figure 5e). The upper boundary is identified as the shallowest depth, z_1, at which Profile E exceeds a chosen threshold value.

Applying this approach to synthetic seismograms shows that a threshold value of 1.5 optimally identifies the upper boundary of the pycnocline where Θ, S_A and ρ_θ most rapidly vary. To identify the lower boundary of the band, the value of Profile D at any

©2020 American Geophysical Union. All rights reserved.

depth is normalized by the mean value of the profile at all greater depths to give Profile F (Figure 5f). The lower boundary is identified as the greatest depth, z_2, at which Profile F exceeds a chosen threshold value. A threshold value of 2.0 is determined by carrying out tests upon synthetic seismograms. Estimated uncertainties for z_1 and z_2 are assigned by identifying the depth range over which contiguous values on profiles E and F vary away from the chosen threshold values by ± 0.5. It is important to note that these uncertainties give only an indication of the sharpness of change in seismic amplitude with depth and they should not be regarded as formal estimates. We have not quantified these uncertainties more robustly since they have an insignificant effect upon subsequent analysis.

We apply this algorithm to 26 synthetic seismograms calculated from CTD casts in order to constrain the density structure of the seismically imaged pycnocline. Values of ρ_θ and N within each of the 26 identified pycnoclines are averaged to yield mean pycnoclinic values of $\langle \rho_\theta \rangle_p = 1027.8 \pm 0.3$ kg m^{-3} and $\langle N \rangle_p = 2.0 \pm 0.3$ cph, respectively. The average potential density of waters above the pycnocline (i.e. FSCUW) is $\bar{\rho}_{\theta_1} = 1027.6 \pm 0.3$ kg m^{-3}. The total change in potential density across the pycnocline, $(\Delta\rho_\theta)_p$, is 0.6 ± 0.1 kg m^{-3}. These values are tabulated in Table 1.

4.2 Tilt Measurements

Reflection tilt between depths of z_1 and z_2 is calculated by tracking reflections that are greater than 2 km long. These reflections are tracked by contouring a constant value of the cosine of the instantaneous phase angle, a seismic attribute which emphasizes reflective continuity (Barnes, 2007). The value of this attribute is unaffected by seismic amplitude and so continuous faint reflections are tracked just as reliably as brighter reflections. Tracked reflections that are shorter than 2 km are discarded. We found that this cut-off length provides an optimal compromise between capturing long-wavelength tilt and tracking a sufficient number of reflections. Transect B23 has only two trackable reflections and so it is excluded from further analysis. For all other transects, the number of tracked reflections on each image varies between 14 and 123. The total length of tracked reflections is 7,650 km.

Straight lines are fitted to tracked reflections using least squares linear regression. The gradient of each tracked reflection, $\tan(\gamma)$, is computed, where γ is the angle between

©2020 American Geophysical Union. All rights reserved.

the reflection and a geopotential surface (i.e. the horizontal level). On each seismic image, individual gradients are averaged to yield a weighted estimate of the mean gradient, $\langle \tan(\gamma) \rangle_p$ within the identified pycnocline (Figure 6). When calculating $\langle \tan(\gamma) \rangle_p$, values of $\tan(\gamma)$ corresponding to longer reflections, which better capture long-wavelength tilt, are more heavily weighted. Values of $\langle \tan(\gamma) \rangle_p < 0$ correspond to reflections that tilt down toward the southwest (i.e. negative tilt). Values of $\langle \tan(\gamma) \rangle_p > 0$ correspond to reflections tilting down toward the northeast (i.e. positive tilt). Measured values of $\langle \tan(\gamma) \rangle_p$ lie within the range -1.25×10^{-2} to 1.75×10^{-2}, which corresponds to $|\gamma| \lesssim 1°$. Standard deviations for $\langle \tan(\gamma) \rangle_p$ fall betwen 0.25×10^{-2} and 1.3×10^{-2}.

These values are computed by implicitly assuming that the imaged structures remain stationary over the period of ~ 1 hour taken to acquire a seismic transect. We readily acknowledge that thermohaline structure can vary significantly on this time scale. For instance, internal tides within the Faroe-Shetland Channel displace isopycnal surfaces over a vertical distance of $\lesssim 50$ m over the course of 1 hour (Knudsen, 1911; T. Sherwin, 1991; T. J. Sherwin, 1995). Current speeds of up to ~ 0.9 m s^{-1} have been recorded (e.g. T. J. Sherwin et al., 2006). A simple model is used to investigate the possible effects that this advection has upon the imaged fine-scale structure (Appendix B.1). This model shows that, for the greatest plausible along-channel (i.e. northeast-southwest) current speed of 1 m s^{-1}, the imaged reflection gradients can differ from actual gradients of reflective surfaces by up to 50%. In reality, this effect is probably much smaller. It is also important to emphasize that advection of fine-scale structure only changes the magnitude of $\tan(\gamma)$. The sense of tilt is unaffected.

Provided that reflections mostly track isopycnal surfaces, $\langle \tan(\gamma) \rangle_p$ provides a measure of the horizontal pressure gradient within the pycnocline. This pressure gradient is balanced by a combination of inertial forces and the Coriolis force (e.g. Simpson, Dickey, & Koblinsky, 1984). Using a two-layer model, we estimate that the Rossby radius of deformation, L_R, is approximately 13 km within the Faroe-Shetland Channel (Appendix B.2; Gerkema, 1996).

The seismic images are $\lesssim 9$ km long. Therefore, it is possible that dipping reflections correspond to slices through a geostrophically balanced mesoscale structure with a length scale that is much greater than L_R. Alternatively, dipping reflections could be caused by sub-mesoscale variations on length scales approximately equal to or shorter

©2020 American Geophysical Union. All rights reserved.

than L_R. At these shorter scales, geostrophy is invalid. Instead, horizontal motion is maintained by a balance between pressure gradients, inertial forces and the Coriolis force (e.g. Simpson et al., 1984). If the Coriolis force contributes significantly to this balance, it must act in the opposite direction to that of the pressure gradient. Even if geostrophy is not an appropriate approximation, tilted reflections are thus indicative of the sense of cross-channel shear between FSCUW and FSCBW. $\langle \tan(\gamma) \rangle_p < 0$ implies that FSCUW is flowing southeastward relative to FSCBW. $\langle \tan(\gamma) \rangle_p > 0$ implies that FSCUW is flowing northwestward relative to FSCBW.

Assuming geostrophy, the change in the out-of-plane (i.e. northwest-southeast) component of geostrophic velocity across the pycnocline can be calculated (Appendix B.3; Sheen et al., 2011; Tang, Gulick, & Sun, 2014). Estimated values of $(\Delta U_p)_\perp$ lie within the range of -0.7 to 1.0 m s^{-1} with uncertainties of ± 0.5 m s^{-1}. It is important to emphasize that we do not use these values for subsequent analysis since the validity of the geostrophic approximation remains uncertain.

4.3 Turbulent Mixing

Diapycnal diffusivity, K, is generally used to parametrize the strength of mechanical mixing that is key to global overturning (Montgomery, 1939; Munk, 1966). We estimate K by first computing the rate of dissipation of turbulent kinetic energy, ϵ, from the turbulent spectral subrange of tracked seismic reflections (e.g. Falder et al., 2016; Holbrook et al., 2013; Sheen, White, & Hobbs, 2009). Before tracking reflections, we minimize the effect of ambient and harmonic noise by following the recommendations of Holbrook et al. (2013) described in Appendix C.1.

Once the effects of noise have been minimized, power spectral densities of vertical displacement are computed from tracked reflections that lie between depths of z_1 and z_2. As before, reflections are tracked by contouring a constant value of the cosine of the instantaneous phase angle (Barnes, 2007). Turbulent motions are expected on horizontal length scales of $\lesssim O(100)$ m (Riley & Lindborg, 2008). Here, we found that tracking reflections longer than 2 km provided the best compromise between tracking a sufficient number of reflections and resolving the shape of the spectrum down to wavenumbers that are smaller than 10^{-3} cycles per meter (cpm). Tracked reflections are linearly detrended in order to remove the long-wavelength signal caused by balanced motions.

©2020 American Geophysical Union. All rights reserved.

Vertical displacements are converted from two-way travel time into depth displacement, ξ, by assuming a constant sound speed of 1480 m s^{-1}. The uncertainty introduced by this assumption is $\lesssim 2\%$ (Dickinson et al., 2017).

Power spectra corresponding to individual reflections are calculated by computing fast Fourier transforms for half-overlapping segments of length 320 points that have been tapered with a Hann window (Welch, 1967). These spectra are computed under the assumption that imaged fine-scale structure is stationary for the duration of the time window taken to acquire all signals that contribute to a given tracked reflection. If fine-scale structure is not stationary, a finite sampling speed acts to smear variability in frequency space into variability in horizontal wavenumber space (Klaeschen, Hobbs, Krahmann, Papenberg, & Vsemirnova, 2009). A model based upon physically reasonable values of buoyancy frequency demonstrates that turbulent motions at wavenumbers greater than 10^{-2} cpm are insignificantly affected by such smearing (Appendix C.2).

In order to improve the signal-to-noise ratio, all of the spectra from a single image are averaged to yield a mean spectrum, $\langle \phi_\xi \rangle_p$, which is representative of all tracked vertical displacements between depths of z_1 and z_2 (Figure 6c,f,i). Averaging spectra in this way obscures the spatial distribution of localized mixing at smaller scales but increases the reliability of the estimated bulk diffusivity for the entire pycnocline. We choose to average spectra in $\log_{10}(\phi_\xi)$ space since previous observations suggest ϵ may have a log-normal distribution in time and space throughout the oceans (e.g. Baker & Gibson, 1987; Gregg, 1980, 1987; Gregg, Seim, & Percival, 1993; Yamazaki & Lueck, 1990). Averaging in linear space increases the magnitude of estimated values of $\log_{10}(K)$ by ~ 0.5 logarithmic units. Nonetheless, the pattern of variation is unaffected. Values of $\langle \phi_\xi \rangle_p$ are converted into spectra of the horizontal gradient of vertical displacement, $\langle \phi_{\xi_x} \rangle_p$, using $\langle \phi_{\xi_x} \rangle_p = (2\pi k_x)^2 \langle \phi_\xi \rangle_p$. After this conversion, turbulent subranges have a slope of $+1/3$ in $\log_{10}(k_x)$–$\log_{10} \langle \phi_{\xi_x} \rangle_p$ space.

These subranges are identified by fitting a model to each mean spectrum in $\log_{10}(k_x)$–$\log_{10} \langle \phi_{\xi_x} \rangle_p$ space (Appendix C.3; Falder et al., 2016). Identified subranges are selected for further analysis provided that they contain at least ten data points. Spectra are deemed to be good quality if the gradient of a straight line fitted to the subrange in $\log_{10}(k_x)$–$\log_{10} \langle \phi_{\xi_x} \rangle_p$ space using linear regression is $+1/3 \pm 0.3$. This degree of subjectivity can

©2020 American Geophysical Union. All rights reserved.

be avoided by adopting more rigorous schemes although the results are unlikely to be materially affected (e.g. B. Ruddick, Anis, & Thompson, 2000).

Good-quality turbulent spectral subranges all lie within the wavenumber range $\sim 10^{-2}$ cpm $\lesssim k_x \lesssim 10^{-1.4}$ cpm, corresponding to horizontal length scales of $\sim$ 25–100 m. These length scales are too great for the signal to correspond to isotropic turbulence. Instead, these observed turbulent subranges probably belong to the regime of layered anisotropic stratified turbulence (LAST; Falder et al., 2016; Riley & Lindborg, 2008). Since there should be continuity between the LAST and inertial-convective regimes, the dissipation rate of turbulent kinetic energy, ϵ, can be estimated by using the inertial-convective parametrization for a passive scalar (Sreenivasan, 1996). If turbulent motions affect temperature in the same way as they affect density, this parametrization can be expressed as

$$\langle \phi_{\xi_x} \rangle_p = \frac{4\pi\Gamma}{N^2} C_T \epsilon^{2/3} (2\pi k_x)^{+1/3}, \tag{1}$$

where Γ is the turbulent flux coefficient and C_T is the Obukhov-Corrsin constant (Falder et al., 2016; Klymak & Moum, 2007b). Diapycnal diffusivity, K, is estimated from ϵ using the Osborn relationship

$$K = \frac{\frac{g}{\rho}\langle w'\rho' \rangle_p}{\frac{-g}{\rho}\frac{d\rho}{dz}} = \frac{B}{N^2} = \frac{\Gamma\epsilon}{N^2}, \tag{2}$$

where g is gravitational acceleration, ρ is mean density, ρ' is density perturbation, w' is vertical component of the velocity perturbation and B is buoyancy flux (Osborn, 1980). Angular brackets denote averaging over time. This equation assumes a balance between turbulent production, dissipation, and work done against buoyancy for the case of a statistically steady flow. The Osborn relationship is also assumed in derivation of Equation (1). By combining Equations (1) and (2), we obtain

$$\log_{10}(K) = \frac{3}{2}\hat{c} - \frac{1}{2}\log_{10}(\Gamma) + \log_{10}(N) - \frac{3}{2}\log_{10}(C_T) - \frac{7}{2}\log_{10}(2) - 2\log_{10}(\pi), \tag{3}$$

where $\hat{c}$ is the intercept of a straight line of gradient $+1/3$ fitted in $\log_{10}(k_x)$–$\log_{10}\langle \phi_{\xi_x} \rangle_p$ space using least squares linear regression. $\log_{10}(K)$ is estimated by assuming that $N = \langle N \rangle_p$ and by taking conventional values of $\Gamma = 0.2$ and $C_T = 0.4$ (Osborn, 1980; Sreenivasan, 1996). Estimated values of K lie in the range $\sim 10^{-5.7}$–$10^{-5.0}$ m^2 s^{-1}.

Uncertainties in the estimated values of K depend upon $\hat{c}$, N, Γ and C_T. The uncertainty for $\hat{c}$ is gauged from standard deviations of the values of $\log_{10}\langle \phi_{\xi_x} \rangle_p$. Note that values of $\sigma_{\hat{c}}$ do not account for deviation of the gradient of $\log_{10}\langle \phi_{\xi_x} \rangle_p$ away from $+1/3$.

©2020 American Geophysical Union. All rights reserved.

Estimated uncertainties in $\hat{c}$ and $\langle N \rangle_p$ are combined in quadrature to yield corresponding uncertainties in $\log_{10}(K)$ of ~ 0.07–0.17 logarithmic units. We assume that $\langle N \rangle_p = 2.0 \pm 0.3$ cph is an appropriate estimate of the mean buoyancy frequency within the pycnocline for the vertical length scales over which turbulent mixing takes place. In determining the effect of uncertainties in Γ and in C_T, we do not formally propagate errors since the underlying probability distributions are not accurately known. Instead, we consider the effects of taking upper and lower bounds of their observed ranges of $0.1 \lesssim \Gamma \lesssim 0.4$ and $0.3 \lesssim C_T \lesssim 0.5$ (Mashayek et al., n.d.; Sreenivasan, 1996). Corresponding uncertainties in $\log(K)$ are ± 0.15 logarithmic units and ± 0.1 logarithmic units, respectively. We conclude that values of $\log_{10}(K)$ are accurate to within one half of an order of magnitude. Further details of our approach to error analysis are described in Appendix C.4.

5 Temporal Evolution of Pycnocline

Evolution of upper pycnoclinic depth, z_1, of lower pycnoclinic depth, z_2, of mean reflection gradient, $\langle \tan(\gamma) \rangle_p$, and of K for Sectors A and B is shown in Figure 7. z_1 is often poorly defined due to the diffuse nature of the upper boundary. The lower boundary, in contrast, is clearly defined and z_2 matches sharp changes of seismic amplitude. The thickness of the band of bright reflections remains reasonably constant (250–400 m). We conclude that z_2 is a satisfactory proxy for the depth of the pycnocline, which is assumed to maintain a constant thickness. Absolute depth of the pycnocline is unimportant for the analysis described below.

Between Days 208 and 212, the lower boundary of the pycnocline is imaged at a depth of $\sim$ 400–500 m within Sector A. The pycnocline then deepens at an average rate of ~ 35 m day^{-1} between Day 215 and Day 225. As the pycnocline deepens, negatively tilted reflections steepen from $|\langle \tan(\gamma) \rangle_p| \sim 0.001$ to $|\langle \tan(\gamma) \rangle_p| \sim 0.012$, indicative of flow with an increasing component toward the southeast. When the pycnocline reaches a maximum depth of ~ 800 m around Day 225, a change in reflection gradient suggests a reversal in the cross-channel flow direction. Between Days 225 and 232, the pycnocline shoals at an average rate of ~ 25 m day^{-1} and the presence of positively tilted reflections suggests a northwestward component of flow. Tilt of these reflections decreases with time from $|\langle \tan(\gamma) \rangle_p| \sim 0.012$ to $|\langle \tan(\gamma) \rangle_p| \sim 0.004$, implying a concomitant decrease in flow speed. Sector B reveals a closely similar pattern of temporal variation in z_2 and $\langle \tan(\gamma) \rangle_p$. However, z_2 reaches its maximum value within Sector B approximately 2 days

©2020 American Geophysical Union. All rights reserved.

Accepted Article

before it reaches its maximum value within Sector A. Likewise, the flow reversal suggested by $\langle \tan(\gamma) \rangle_p$ occurs $\sim$ 2 days earlier in Sector B. Close correspondence between variation in pycnoclinic depth and variation in reflection tilt suggests that the two observations are correlated. Once again, we emphasize that these variations are caused by temporal changes in thermohaline structure over the 25 days taken to acquire the seismic survey. Moreover, the similarity of temporal variations between both sectors suggests that the physical mechanism causing these variations has a spatial scale that is much larger than the scale of the seismic survey. The time lag of ~ 2 days between Sectors B and A suggests that observed changes do, however, have at least a weak spatial dependence over the length scale of the survey.

Temporal changes in calculated values of K show some relation to variations in z_2 and $\langle \tan(\gamma) \rangle_p$. Between Days 215 and 225, values of K for Sector B decrease from $\sim 10^{-5.0}$ m^2 s^{-1} to $\sim 10^{-5.5}$ m^2 s^{-1}. After Day 225, K steadily increases from $\sim 10^{-5.5}$ m^2 s^{-1} to $\sim 10^{-5.2}$ m^2 s^{-1}. Sector A has a similar suppression of K at around Day 225. However, we note that there is significant scatter in these trends.

5.1 Qualitative Interpretation

Two mechanisms dominate intermittent deviations from the mean flow within the Faroe-Shetland Channel. First, cold-core eddies with diameters of 30–50 km have been observed (Hansen & Meincke, 1979; T. J. Sherwin et al., 1999). Secondly, the Continental Slope Current can migrate towards the center of the channel where it forms meanders with length scales of 30–70 km (H. D. Dooley & Meincke, 1981; T. J. Sherwin et al., 1999, 2006). Both of these mechanisms have the potential to cause swirling motions that are well described by a rotating lens of fluid with vertical vorticity (i.e. a vortex). Measurements of the dynamics and hydrography of oceanic vortices have often been recorded in terms of radial distance from the center of the vortex (e.g. Olson, Schmitt, Kennelly, & Joyce, 1985).

The seismic transects presented here provide a series of measurements of z_2 and $\langle \tan(\gamma) \rangle_p$ at different locations and times. It is not straightforward to express these measurements in terms of distance from the center of a vortex. However, measurements can be related to the orientation and sense of flow of the vortex. Isopycnal surfaces are depressed and elevated toward the center of an anticyclonic vortex and of a cyclonic vor-

Accepted Article

©2020 American Geophysical Union. All rights reserved.

tex, respectively (e.g., Olson, 1991). Translation of a vortex along the channel would therefore generate variations in pycnoclinic depth and in current direction. These variations are manifest on seismic images as changes in z_2 and in $\langle \tan(\gamma) \rangle_p$, respectively. Four cases are illustrated in Figure 8. These cases are denoted by A (for anticyclonic vortex) or C (for cyclonic vortex). NE and SW denote northeastward and southwestward propagation, respectively.

Case C-NE illustrates northeastward translation of a cyclonic vortex (Figure 8a-c). Initially, this vortex is located southwest of the seismic survey and tilted seismic reflections record northwestward flow of FSCUW relative to FSCBW (i.e. $\langle \tan(\gamma) \rangle_p > 0$). As the vortex translates northeastward, seismic transects sample waters closer to the vortex center and the seismically imaged pycnocline shoals (i.e. z_2 decreases). Tilted seismic reflections record increasingly positive $\langle \tan(\gamma) \rangle_p$ as the magnitude of azimuthal velocities increases towards the edge of the core region. As the vortex center passes through the region of the seismic survey, the observed pycnocline reaches its minimum depth and $\langle \tan(\gamma) \rangle_p$ decreases to near zero as the strength of azimuthal flow reduces within the core region. At later times, the vortex center is to the northeast of the seismic survey. Flow of FSCUW relative to FSCBW is thus to the southeast (i.e. $\langle \tan(\gamma) \rangle_p < 0$). The observed pycnocline deepens as distance from the vortex center increases. Cases C-SW, A-NE and A-SW are illustrated in panels d-f, g-i and j-l of Figure 8, respectively. Comparison with recorded values of z_2 and of $\langle \tan(\gamma) \rangle_p$ shows that case A-NE is consistent with observations.

5.2 Fitting of Model Vortices

Based on this interpretation, we fit a dynamical model of a northeastward-translating anticyclonic vortex to observed values of z_2 and $\langle \tan(\gamma) \rangle_p$. A circular vortex has azimuthal velocity, $u_\theta(r)$, which depends on radial distance, r, from the vortex center. Vortices in a rotating inviscid fluid are maintained by a gradient balance between the centrifugal force, the Coriolis force, and pressure gradients (e.g. Simpson et al., 1984). Associated azimuthal velocities are known as gradient velocities. At small radial distances (i.e. $|r| \ll L_R$), influence of the centrifugal force cannot be ignored and gradient velocities depart significantly from geostrophic velocities (Carton, 2001). At large radial distances (i.e. $|r| \gg L_R$), the effect of the centrifugal force decreases and motions can be accurately described by geostrophy.

©2020 American Geophysical Union. All rights reserved.

Observations of mid-ocean vortices suggest that the exact radial dependence of $u_\theta(r)$ can vary (e.g. Olson, 1980, 1991; Simpson et al., 1984). However, all vortices feature a core region, within which $u_\theta(r)$ increases with increasing r (Carton, 2001; Hopfinger & van Heijst, 1993). Outside of this core region, far-field values of $u_\theta(r)$ decrease monotonically with increasing r. Based on these observations, a range of dynamically complete models of vortex motion in both two-layer systems and continuously stratified fluids have been developed and experimentally verified (e.g., Cushman-Roisin & Merchant-Both, 1995; Griffiths & Hopfinger, 1987; Rubino, Brandt, & Hessner, 1998). However, these models consider isolated vortices that do not interact with background currents or with steep bathymetry. They are not suited to describing the behavior of a vortex within the confined trough of the Faroe-Shetland Channel.

Here, we use the simplest possible model and so the effects of bathymetry and viscous dissipation are ignored. Radial velocities are also neglected since they are small compared with azimuthal velocities. The Gaussian vortex has a convenient analytical form (Carton, Flierl, & Polvani, 1989). Its azimuthal velocity is given by

$$u_\theta(r) = \frac{1}{2} V_g \frac{r}{R_g} e^{-(r/R_g)^2}, \tag{4}$$

where V_g and R_g are velocity and length scales, respectively. Maximum radial velocity, $u_{\theta m}$, occurs at radius r_m where

$$u_{\theta_m} = \frac{V_g}{2\sqrt{2}e^{1/2}} \tag{5}$$

and

$$r_m = \frac{R_g}{\sqrt{2}}. \tag{6}$$

$u_\theta(r)$ represents a gradient velocity, and is related to the radial pressure gradient, $1/\rho(\partial P/\partial r)$, by

$$-\frac{1}{\rho}\frac{\partial P}{\partial r} = \frac{1}{2} V_g \frac{r}{R_g} e^{-(r/R_g)^2} \left(\frac{1}{2} \frac{V_g}{R_g} e^{-(r/R_g)^2} + f \right). \tag{7}$$

In order to compare seismic observations to this model, isopycnal tilt (i.e., $\langle \tan(\gamma) \rangle_p$) and pycnoclinic depth (i.e. z_2) are related to the radial pressure gradient. To do so, the density structure in the Faroe-Shetland Channel is approximated using a two-layer fluid, in which z_2 represents the sharp interface that separates an upper layer of FSCUW from a lower layer of FSCBW. The density contrast between these two layers is given by $\langle \Delta\rho_\theta \rangle_p$ and the density of the upper layer is $\bar{\rho}_{\theta_1}$. In this approximation, the radial pressure gradient can be related directly to isopycnal tilt by assuming a linear scaling that is given

©2020 American Geophysical Union. All rights reserved.

Accepted Article

by

$$\langle \tan(\gamma) \rangle_p = \frac{b}{\bar{\rho}_{\theta_1} g'} \left(\frac{\partial P}{\partial r} \right)_{||}, \tag{8}$$

where b is a dimensionless constant and $||$ denotes the component within the plane of the seismic image. For this scaling, Equation (7) can be directly fitted to $\langle \tan(\gamma) \rangle_p$, regardless of the magnitude of b. However, a more specific scaling is required to model the observed variation of z_2. A well-known approximation is to assume that the barotropic mode is compensated by the baroclinic mode in the lower layer, which remains at rest (i.e. $b = 1$; e.g., Olson et al., 1985). This approximation, which is known as the $1\frac{1}{2}$-layer ocean, is probably sufficiently accurate for cases where the lower layer is much deeper than the upper layer (e.g. Carton, 2001; Olson et al., 1985). It does not provide a complete description of the density structure within the Faroe-Shetland Channel, where the upper layer of FSCUW and the lower layer of FSCBW have approximately equal thicknesses. Nevertheless, we make use of this $1\frac{1}{2}$-layer ocean approximation since, given the physically complex interactions of currents and bathymetry within the Faroe-Shetland Channel, its simplicity yields greater physical insight than more complex models. It is important to note that the $1\frac{1}{2}$-layer ocean model is only used to fit values of z_2. It is not used to fit values of $\langle \tan(\gamma) \rangle_p$.

For the $1\frac{1}{2}$-layer ocean model, pressure gradients caused by variations in sea-surface height are balanced by pressure gradients caused by displacement of the interface separating upper and lower layers. Interface depth, h, is thus related to sea-surface height anomaly, η, by

$$h = \frac{\bar{\rho}_{\theta_1}}{\langle \Delta\rho_\theta \rangle_p} \eta + h_\infty, \tag{9}$$

where h_∞ is unperturbed interface depth. h can be expressed in terms of the radial pressure gradient using

$$\frac{dh(r)}{dr} = -\frac{1}{\bar{\rho}_{\theta_1} g'} \frac{\partial P}{\partial r}. \tag{10}$$

In the case of a Gaussian vortex, $dh(r)/dr$ and $h(r)$ are given by

$$\frac{dh(r)}{dr} = \frac{1}{2g'} V_g \frac{r}{R_g} e^{-(r/R_g)^2} \left(\frac{1}{2} \frac{V_g}{R_g} e^{-(r/R_g)^2} + f \right) \tag{11}$$

and

$$h(r) = \frac{\sqrt{\pi}}{16g'} V_g^2 \ \mathrm{erf}\left(\frac{r^2}{R_g^2} \right) - \frac{f}{4g'} V_g R_g e^{-(r/R_g)^2} + h_\infty, \tag{12}$$

where $\mathrm{erf}(x)$ is the error function. Modeled values of dh/dr and h can be fitted to measurements of $\langle \tan(\gamma) \rangle_p$ and z_2, respectively. Equations (11) and (12) have three free parameters (i.e. R_g, V_g, h_∞). However, these equations also contain f and g', which must

©2020 American Geophysical Union. All rights reserved.

first be estimated. To avoid errors in estimated values of f and g' affecting the fitting, it is assumed that geostrophy applies. Equations (11) and (12) then become

$$\frac{dh(r)}{dr} = \frac{V_1 r}{R_g} e^{-(r/R_g)^2} \tag{13}$$

and

$$h(r) = -\frac{1}{2} V_1 R_g e^{-(r/R_g)^2} + h_\infty, \tag{14}$$

where $V_1 = (fV_g)/(2g')$. f and g' are now contained within the free parameter V_1, which is fitted to observations. Fitting of the full gradient balance using Equations (11) and (12) makes little difference.

We initially attempted to fit values of $\langle \tan(\gamma) \rangle_p$ and z_2 using Equations (13) and (14) by exploiting spatial variations between adjacent seismic transects. However, the results were sensitive to initial conditions and global minima of the misfit spaces were not well constrained. In order to simplify the problem, observations are fitted using Equations (13) and (14) by assuming that the model vortex translates parallel to the seismic transects. It is also assumed that the vortex radius is much greater than the region covered by the seismic survey. In this case, all seismic transects can be regarded as having been acquired in the same location. It is furthermore assumed that the vortex center passes through this location. Recorded values of $\langle \tan(\gamma) \rangle_p$ and z_2 thus correspond to radial profiles of dh/dr and h, respectively. $\langle \tan(\gamma) \rangle_p$ and z_2 are measured as functions of time, t. t is related to distance from vortex center, r, by $t = (t_0 + (r/u_t))$, where u_t is constant translational speed of the vortex and t_0 is time at which the vortex center passes through the seismic survey. Equations (13) and (14) are expressed in terms of t by

$$\frac{dh(t)}{dr} = \frac{V_1 t}{T_g} e^{-(t/T_g)^2} \tag{15}$$

and

$$h(t) = -\frac{1}{2} V_1 u_t T_g e^{-(t/T_g)^2} + h_\infty, \tag{16}$$

where $T_g = R_g/u_t$. First, $dh(t)/dr$ is fitted to $\langle \tan(\gamma) \rangle_p$ by defining the misfit function

$$M_1 = \sqrt{\frac{1}{D-F} \sum_{i=1}^{D} \left[\frac{\left(\langle \tan(\gamma) \rangle_p \right)_i - (dh(t)/dr)_i}{\left(\sigma \langle \tan(\gamma) \rangle_p \right)_i} \right]^2}, \tag{17}$$

where $D = 54$ is number of data points, F is number of free parameters and $\sigma \langle \tan(\gamma) \rangle_p$ is the standard deviation on $\langle \tan(\gamma) \rangle_p$. M_1 is minimized using a conjugate direction search algorithm (M. J. D. Powell, 1964). Optimization depends on three free parameters (t_0,

©2020 American Geophysical Union. All rights reserved.

T_g and V_1) and best-fitting values of $t_0 \approx 1.47\times10^6$ s, $V_1 \approx 2.3\times10^{-2}$ and $T_g \approx 2.6\times 10^5$ s are recovered (Figure 9b). The fit is good ($M_1 \approx 0.9$) and parameter sweep around the best-fitting values shows that the minimum is well defined (Figure 9c-e). This fit does not depend on assumption of the 1-$\frac{1}{2}$-layer ocean model. Instead, as discussed above, it simply depends on a linear scaling between $\langle\tan(\gamma)\rangle_p$ and the in-plane component of the radial pressure gradient. However, neither u_t nor h_∞ can be estimated by fitting $\langle\tan(\gamma)\rangle_p$ alone. u_t and h_∞ are estimated by fixing $t_0 = 1.47\times10^6$ s, $V_1 = 2.3\times10^{-2}$ and $T_g = 2.6\times10^5$ s, and varying u_t and h_∞ to minimize the misfit function

$$M_2 = W\sqrt{\frac{1}{D-F}\sum_{i=1}^{D}\left[(z_2)_i - (h(t))_i\right]^2}, \tag{18}$$

where W is a weighting factor. Errors on z_2 are arbitrary and so M_2 is not weighted by these errors. The value of W is chosen to bring misfit values closer to 1. Best-fitting values of $u_t \approx 6.9\times10^{-2}$ m s^{-1} and $h_\infty \approx 570$ m are recovered. The fit is satisfactory between Day 220 and Day 230 (Figure 9a). However, slices through the misfit space indicate that the minimum is not tightly constrained for all parameters. T_g and V_1 are converted into estimates of $R_g \approx 18$ km and $V_g \approx 2.1$ m s^{-1} using $u_t = 6.9\times10^{-2}$ m s^{-1}, $f = 1.29\times10^{-4}$ s^{-1} and $\Delta\rho = \langle\Delta\rho_\theta\rangle_p = 0.6$ kg m^{-3}. Equations (5) and (6) then yield $r_m \approx 13$ km and $u_{\theta_m} \approx 0.44$ m s^{-1}. Errors are not formally estimated since the model of a translating vortex is necessarily simplistic. The largest source of error is probably the assumption that all transects were acquired at the same location.

Secondly, $h(t)$ is solely fitted to z_2 using the misfit function M_2 (Figure 9f). Measurements of $\langle\tan(\gamma)\rangle_p$ are not exploited. This fit constrains all five model parameters (i.e. t_0, T_g, V_2, u_t, h_∞). The weighting factor W is again set to a value that brings misfit values closer to 1. Best-fitting values of $t_0 \approx 1.52\times10^6$ s, $T_g \approx 7.2\times10^5$ s, $V_1 \approx 8.3\times10^{-3}$, $u_t \approx 8.5\times10^{-2}$ m s^{-1} and $h_\infty \approx 470$ m are recovered and the minimum is well defined (selected slices through the misfit space are shown in Figure 9h-j). However, values of $dh(t)/dr$ computed using these fitted values do not compare well to $\langle\tan(\gamma)\rangle_p$ (Figure 9g). In particular, fitting of z_2 requires a vortex with a core radius that is much greater than one required to fit $\langle\tan(\gamma)\rangle_p$. T_g, V_1 and u_t are converted into estimates of $R_g \approx 61$ km, $r_m \approx 43$ km and $u_{\theta_m} \approx 0.16$ m s^{-1}.

©2020 American Geophysical Union. All rights reserved.

5.3 Coincident Satellite Observations

These modeling results can be interpreted with the aid of independent satellite observations in several different ways. First, we exploit images of sea-surface temperature acquired by the Advanced Very High Resolution Radiometer (AVHRR) of the NOAA-14 satellite. Five clear images were obtained during the period of seismic acquisition (Figure 10a-d,f). These images are constructed using records acquired by $\lesssim 8$ satellite passes over the course of a single day. Absolute temperatures are accurate to only ~ 1°C (e.g. Keogh, Robinson, Donlon, & Nightingale, 1999; Park et al., 2015). Nonetheless, these images reveal broad changes in the location of the front that separates cooler MNAW from warmer NAW. Between Days 212 and 224, the Continental Slope Current appears to move toward the center of the channel. By Day 229, this excursion has developed into an approximately circular swirling warm-water structure with a diameter of ~ 150 km whose center is close to 61° N and 4° W. After the window of seismic acquisition, this structure persists until at least Day 245 (Figure 10i,j,l,n).

We then examine sea-surface height measurements acquired by the TOPEX/Poseidon satellite, which followed a ground track that runs close to the axis of the channel and passes the location of the seismic survey (Figure 10e,g,i). Measurements were taken once every 10 days at an along-track spacing of $\sim$ 6.2 km. Records acquired on Days 206, 226, 236, 246 and 256 are examined. Unfortunately, records are unavailable for Day 216, which, along with Day 226, overlap the window of seismic acquisition. Each pass took ~ 1 minute to acquire measurements at the locations shown in Figure 10 so that these measurements can be regarded as instantaneous. After they have been corrected for sources of error such as ionospheric delay and inaccuracies in orbital height of the altimeter, the measurements have absolute uncertainties of $\pm(5\text{–}10)\times10^{-2}$ m (Naeije et al., 2002; Stammer & Wunsch, 1994). On horizontal length scales of $\lesssim 100$ km, these uncertainties are approximately constant and do not significantly affect signals of mesoscale structure (Leben & Powell, 2003; Yale, Sandwell, & Smith, 1995). Observed anomalies are smoothed using a 7-point Hann filter to remove small-scale ageostrophic signals and ambient noise (Darelius, Ullgren, & Fer, 2013).

The smoothed anomalies, η_7, are analyzed in two ways. First, the cross-track (i.e. northwest-southeast) component of the geostrophic velocity field, $u_{sg_\perp}$, is estimated. Different schemes for estimating geostrophic velocities from sea-surface height anomalies

©2020 American Geophysical Union. All rights reserved.

have been proposed (e.g. B. S. Powell & Leben, 2004). Here, we employ a first-order finite-difference scheme that accurately resolves gross features of mesoscale flow on length scales of order 30 km (Lilly et al., 2003). The value of $u_{sg_\perp}$ at the midpoint of two adjacent measurement locations, separated by an along-track distance Δx, is given by

$$u_{sg_\perp} = -\frac{g}{f}\frac{\Delta\eta_7}{\Delta x}, \tag{19}$$

where $\Delta\eta_7$ is the difference in η_7 between the two measurement locations. Assuming that g, f and Δx are free of error, the fractional error for $u_{sg_\perp}$ is equal to the fractional error for $\Delta\eta_7$. Assuming that absolute uncertainties in $\Delta\eta_7$ are $\pm(5\text{–}10) \times 10^{-2}$ m, the estimated errors in $u_{sg_\perp}$ are of order 0.1 m s^{-1}.

Values of $u_{sg_\perp}$ computed for Day 226 suggest a region of anticylonic flow of peak-to-peak distance $\sim$ 50 km (Figures 10e). The center of this vortex, where $u_{sg_\perp}$ is close to $\sim$ 0 m s^{-1}, lies close to the seismic survey. This flow is more clearly defined on Day 236 when anticyclonic motion with $u_{sg_\perp}$ of up to $\sim$ 0.25 m s^{-1} overlies the swirling structure observed on AVHRR imagery (Figures 10g). Measurements obtained on Day 246 suggest that cross-channel velocities continue to strengthen to $\sim$ 0.3 m s^{-1} (Figure 10i).

Secondly, sea-surface height anomalies are used to estimate changes in pycnoclinic depth. Wunsch (1997) finds that sea-surface height corresponds reasonably well to the depth of the main pycnocline throughout most of the oceans. For the $1\frac{1}{2}$-layer ocean model, interface depth, h, is related to sea-surface height anomaly, η, by Equation (9). h is computed using $\eta = \eta_7$. Depth of the unperturbed pycnocline, h_∞, cannot be estimated from sea-surface height anomalies and is arbitrarily set to 400 m in order to facilitate comparison with z_2. Numerical errors for h are estimated by assuming that errors for $\bar{\rho}_{\theta_1}$, $\langle\Delta\rho_\theta\rangle_p$ and η_7 are normally distributed, and that the error for η_7 is 5×10^{-2} m. Combination of these errors in quadrature yields an uncertainty for h of about $\pm$100 m. This uncertainty does not take account of the suitability of the $1\frac{1}{2}$-layer ocean model. Values of h that are computed for Day 226 are given on the right-hand axis of Figure 11a. Close to the seismic survey, h increases by $\sim$ 250 m between Days 206 and 226. This deepening compares favorably with an increase of $\sim$ 350 m in the value of z_2. Days 236, 246 and 256 reveal a similar signal with values of h close to the seismic survey remaining depressed by $\sim$ 250–350 m relative to Day 206.

Finally, we quantitatively analyse these altimetric records by fitting Gaussian vortices to the values of $u_{sg_\perp}$ computed for Days 226, 236, 246 and 256. In Figure 11b-e,

©2020 American Geophysical Union. All rights reserved.

Day 226 is shown as an example. It is assumed that estimated values of $u_{sg_\perp}$ correspond to a radial profile of azimuthal velocity through the vortex. Observations chosen to be fitted are selected based upon changes in the sign of $u_{sg_\perp}$ at the edges of the anticyclonic region. A misfit function, M_3, is defined as

$$M_3 = \sqrt{\frac{1}{D-3}\sum_{i=1}^{D}\left[\frac{u_{sg_\perp}(x_1)_i - u_\theta(r)_i}{\sigma\left(u_{sg_\perp}(x_1)\right)_i}\right]^2}, \tag{20}$$

where $D = 19$ is number of data points, $x_1 = (x - x_0)$ where x is along-track distance and x_0 corresponds to vortex center, and $u_\theta(r)$ is computed using Equation (4). A global minimum is identified by parameter sweep. Slices through the misfit space reveal that values of the free parameters $x_0 = 183$ km, $R_g = 27$ km and $V_g = 1.2$ m s^{-1} are not well constrained due to observational scatter (Figure 11b-d). R_g and V_g are converted into values of $r_m \approx 19$ km and $u_{\theta_m} \approx 2.6 \times 10^{-2}$ m s^{-1}, respectively, using Equations (5) and (6). Vortices fitted to $u_{sg_\perp}$ for Days 236, 246 and 256 confirm that anticyclonic motion continues to strengthen and by Day 256, the values of R_g and u_{θ_m} reach ~ 47 km and ~ 0.36 m s^{-1}, respectively. Visual inspection of altimetric records suggests that between Day 226 and Day 256 the center of the observed vortex is being advected northeastward at an along-channel speed of ~ 0.01 m s^{-1}.

6 Discussion

A combination of seismic and satellite observations can be used to develop a consistent interpretation of mesoscale activity. First, we consider the limitations of dynamical models that have been fitted to these observations. It has been assumed that motions are described by a Gaussian vortex of constant form that is advected through an inviscid two-layer system. Thus bathymetry and background currents have been neglected. We have further assumed that all measurements sample the vortex along a radial profile so that the spatial variation of altimetric measurements directly corresponds to the temporal variation of seismic records. As a result of these assumptions, the models are unlikely to provide a full description of vortex motion and absolute values of fitted parameters are uncertain.

Despite these limitations, observations and fitted models provide useful insight into dynamical processes within the channel. First, observed changes in z_2 require a vortex with a core radius which is greater than that implied by variations in $\langle \tan(\gamma) \rangle_p$. Values of $\langle \tan(\gamma) \rangle_p$ are more direct indicators of strong azimuthal flow induced by the vortex

©2020 American Geophysical Union. All rights reserved.

and changes in z_2 before Day 218 could be caused by other processes. Fitting a vortex to $\langle \tan(\gamma) \rangle_p$, rather than to z_2, is probably more reliable since it is not necessary to use the 1-$\frac{1}{2}$-layer ocean model. However, fitting values of $\langle \tan(\gamma) \rangle_p$ alone cannot constrain the radius or translational speed of the vortex. Translational speeds estimated from z_2 are $\sim O(0.1)$ m s^{-1}. Satellite altimetric records acquired on Day 226 suggest that the vortex has a radius of ~ 27 km. A Gaussian vortex with this radius would have to translate at ~ 0.1 m s^{-1} in order to generate observed variations in $\langle \tan(\gamma) \rangle_p$. Satellite records also suggest that the size of the vortex increases during the seismic survey. Changes in z_2 and in $\langle \tan(\gamma) \rangle_p$ are probably the result of a combination of growth and advection of the vortex.

The following interpretation is suggested. Between Days 208 and 218, a large volume of near-surface water from the Continental Slope Current moves toward the center of the channel. This movement leads to deepening of the pycnocline, which is recorded on seismic images by an increase in z_2 before Day 218. Deepening occurs over horizontal length scales of $\sim O(100)$ km that are too large to correspond to seismically detectable changes of reflection tilt over along-channel distances of $\lesssim 9$ km. Meandering of Continental Slope Current water also induces formation of an anticyclonic vortex close to the seismic survey. Changes in $\langle \tan(\gamma) \rangle_p$ and in values of z_2 are induced by northeastward advection of this vortex as it strengthens. Both seismic and satellite records indicate that the advective speed falls within the range 0.01–0.1 m s^{-1}. By Day 256, the fully formed vortex appears to have a core radius, R_g, of 40–50 km and a maximum near-surface azimuthal speed, u_{θ_m}, of 0.3–0.4 m s^{-1}. At the center of the vortex, the pycnocline is displaced by a distance, $h(0)$, of 250–350 m.

These values of R_g, u_{θ_m} and $h(0)$ together with values of $\rho = \bar{\rho}_{\theta_1} = 1027.6$ kg m^{-3} and $\Delta\rho = \langle \Delta\rho_\theta \rangle_p = 0.6$ kg m^{-3}, can be used to address the scale and energetics of the observed vortex and its relationship to turbulent mixing. It is assumed that displacement of the pycnocline, $h(r)$, is described by

$$h(r) = h(0)e^{-(r/R_g)^2} + h_\infty. \tag{21}$$

The volume of FSCUW, $V(r < R_g)$, within the core of the vortex is estimated using

$$V(r < R_g) = \int_0^{R_g} h(r) 2\pi r dr. \tag{22}$$

$V(r < R_g)$ is in the range (2.3–4.9)$\times 10^{12}$ m^3. Following Olson et al. (1985), the available potential energy, APE, for the core of a vortex in a two-layer system can be esti-

©2020 American Geophysical Union. All rights reserved.

mated from

$$\mathrm{APE} = \int_0^{R_g} \frac{1}{2}\rho g'(h(r) - h_\infty)^2 2\pi r dr. \tag{23}$$

The calculated value of APE is in the range $\sim$ 0.4–1.2 PJ. Kinetic energy, KE, is given by

$$\mathrm{KE} = \int_0^{R_g} \frac{1}{2}\rho h(r) u_\theta^2(r) 2\pi r dr, \tag{24}$$

where it is assumed that motion is confined to the upper layer and that $u_\theta(r)$ is given by Equation (4) (Olson, 1991). The calculated value of KE falls between 84 and 320 TJ. The total energy of the vortex is therefore $\sim$ 0.5–1.5 PJ.

A component of this energy will be transferred into the internal wave field and dissipated by turbulent motions. The estimated values of K are generally depressed towards the center of the vortex within Sector B (Figure 7h). Two mechanisms could be responsible for this observation. First, it is possible that pycnoclinic waters within the core of the vortex are more strongly stratified than external pycnoclinic waters. Stronger stratification inhibits vertical displacement of isopycnal surfaces, which we regard as a proxy for the strength of turbulent mixing. If N varies by ± 1 cph about 2 cph, estimated values of $\log_{10}(K)$ change by up to 0.26 logarithmic units (Appendix C.4). The trend shown in Figure 7h may thus be partly caused by assuming a constant value of N.

Secondly, changes in calculated values of K could be generated by enhanced shear along the sides of the vortex (Liu et al., 2017; Yang, Zhao, Liang, Dong, & Tian, 2017). With the exception of two measurements acquired around Day 227, elevated values of K do not correspond to elevated values of $\langle \tan(\gamma) \rangle_p$, which are indicative of enhanced shear. This lack of correspondence suggests that regions of high shear do not generate local turbulent dissipation. Instead, energy could be carried away from the core of the vortex by internal waves that break within weaker stratification located away from the core (Tang, Gulick, Sun, Sun, & Jing, 2019). In general, variations in calculated values of K are probably caused by a combination of changes in stratification and in the strength of turbulent mixing that are brought about by passage of the vortex. Few clear turbulent subranges are observed in Sector A where it is not possible to identify a trend in $\log_{10}(K)$ with any confidence (Figure 7d).

Generation and decay of a vortex of this size and energy will significantly affect transport and mixing within the channel. Berx et al. (2013) show that mesoscale fluctuations cause monthly variations of up to $\sim$ 4 Sv in northward transport of water of Atlantic

©2020 American Geophysical Union. All rights reserved.

origin. Within the channel, meandering of the warm, saline Continental Slope Current from the southeast to the northwest side of the channel could have dramatic effects on circulation and fish stocks around the Faroe plateau (e.g. Hansen & Jákupsstovu, 1995). Altimetric observations and images of sea-surface temperature imply that semi-permanent meanders tend to repeatedly form at specific locations (Chafik, 2012; T. J. Sherwin et al., 2006). Development of these meanders is probably forced by a wide range of processes, such as atmospheric variations and intermittent overflow events at the Faroe Bank Channel and across the Wyville Thomson Ridge (e.g. Chafik, 2012; Meincke & Kvinge, 1978; Ullgren, Fer, Darelius, & Beaird, 2014). Eddy-resolving numerical circulation models reproduce some of these observations (Broadbridge & Toumi, 2015; Oey, 1997). In future, an understanding of the formation and longevity of these meanders, as well as their effect on transport at depth, could be improved by ongoing development of eddy-resolving models that are informed by observational time series.

The seismic images described and analyzed here represent a time series that is unprecedented in its ability to link generation and growth of a meander with its influence on submesoscale structure and on turbulent mixing. This study also demonstrates the potential of time-lapse seismic imaging to provide unrivalled observations of the energy cascade over hitherto inaccessible length scales. Both existing and newly acquired seismic records could be used to map interactions between mesoscale and turbulent motions over substantial tracts of the oceanic realm.

7 Conclusions

54 seismic reflection images of thermohaline structure in the deep ($\gtrsim$ 800 m) Faroe-Shetland Channel have been constructed from parallel transects acquired during July-August 1997. These transects were obtained in a sequential manner so that adjacent transects are separated by $\sim$ 300 m in the cross-channel direction and by $\sim$ 1 day in time. The images thus represent a time-lapse series of observations within a small spatial area. A band of bright reflections at depth dominates most images. Comparison with independent CTD casts shows that these reflections are predominantly caused by temperature changes within a pycnocline that separates warm, near-surface waters from cold waters at depth. Temporal changes in pycnoclinic depth and in reflective tilt are quantified by analyzing changes in seismic amplitude and by automatically tracking reflections, respectively. These changes are consistent with northeastward passage of an an-

©2020 American Geophysical Union. All rights reserved.

Accepted Article

ticyclonic vortex through the region of interest. Comparison with coincident satellite measurements of sea-surface temperature and of sea-surface height suggests that this vortex is caused by meandering of the Continental Slope Current. Modeling of these seismic and satellite observations suggests that the fully formed vortex has a radius of 40–50 km, a volume of (2.3–4.9)$\times 10^{12}$ m^3 and an energy of 0.5–1.5 PJ. It is advected northeastward at a speed of 0.01–0.1 m s^{-1}. Spectral analysis of the turbulent subrange of tracked seismic reflections suggests that passage of the vortex may produce changes in the strength of mechanical mixing. However, it is not possible to conclude with any certainty that changes in spectral amplitude are due to variations in the intensity of turbulence rather than to changes in buoyancy frequency. Estimated values of the diapycnal diffusivity, K, fall within the range $10^{-5.7}$–$10^{-5.0}$ m^2 s^{-1}. This seismic study is a novel approach to analyzing the effect of a meander on thermohaline structure at depth within the Faroe-Shetland Channel. Fluxes of heat and salt through the channel will be significantly affected on time scales of months by vortices of this size. Time-lapse three-dimensional seismic reflection surveys are unprecedented in their ability to capture rapid variations in fine-scale structure over horizontal scales of $O(10^1)$–$O(10^4)$ m. This unique ability should permit detailed investigation of the energy cascade that links mesoscale activity to the internal wave field and to turbulent dissipation.

Acknowledgments

A.D. is supported by the Natural Environment Research Council (NERC). Research activity of C.P.C. is supported by Engineering and Physical Science Research Council Program Grant EP/K034529/1 (Mathematical Underpinnings of Stratified Turbulence). We are grateful to PGS ASA for generously providing original seismic field tapes. Access to these tapes can be requested directly from PGS ASA. Signal processing of seismic reflection records was carried out using the Omega2 software package, which was generously provided by Schlumberger Limited. Hydrographic measurements were downloaded from the National Oceanic and Atmospheric Administration (`noaa.gov`). Hydrographic properties were computed using the Python implementation of the GSW TEOS-10 empirical equation of state for seawater (`github.com/TEOS-10/GSW-Python`; IOC et al., 2010). TOPEX/Poseidon altimetric records were downloaded from the Radar Altimeter Database System (RADS; `rads.tudelft.nl/rads/rads.shtml`). AVHRR sea-surface temperature records were supplied by the NERC Earth Observation Data Acquisition and Analysis

©2020 American Geophysical Union. All rights reserved.

Service (NEODAAS; www.neodaas.ac.uk). Bathymetric grid was downloaded from ERDDAP (coastwatch.pfeg.noaa.gov/erddap/index.html). Figures were prepared using the Generic Mapping Tools (gmt.soest.hawaii.edu). We are grateful to Ophelia Crawford for her assistance in calculating synthetic seismograms. We thank K. Gunn, I. Frame and D. Lyness for their help. Cambridge Earth Sciences contribution number esc.XXXX.

Accepted Article

©2020 American Geophysical Union. All rights reserved.

8 Figures

Accepted Article

©2020 American Geophysical Union. All rights reserved.

Accepted Article

Table 1. Commonly used acronyms, constants, variables and non-SI units.

Symbol	Description	Value	Unit	Dimension
Hydrography				
cph	cycles per hour		cph	T^{-1}
FSCBW	Faroe-Shetland Channel Bottom Water			
FSCUW	Faroe-Shetland Channel Upper Water			
N	Buoyancy frequency		cph	T^{-1}
$\langle N \rangle_p$	Estimated buoyancy frequency within pycnocline	2.0 ± 0.3	cph	T^{-1}
S_A	Absolute salinity			g kg^{-1}
Θ	Conservative temperature		°C	Θ
ρ_θ	Potential density		kg m^{-3}	M L^{-3}
$\bar{\rho}_{\theta_1}$	Estimated potential density of FSCUW	1027.6 ± 0.3	kg m^{-3}	M L^{-3}
$\langle \rho_\theta \rangle_p$	Estimated potential density within pycnocline	1027.8 ± 0.3	kg m^{-3}	M L^{-3}
$\langle \Delta\rho_\theta \rangle_p$	Estimated change in potential density across pycnocline	0.6 ± 0.1	kg m^{-3}	M L^{-3}
Seismic Imaging				
cmp	Common midpoint			
R	Reflection coefficient			Dimensionless
u_c	Speed of background current		m s^{-1}	L T^{-1}
u_v	Vessel speed		m s^{-1}	L T^{-1}
z_1	Mean depth of upper boundary of seismically imaged pycnocline		m	L
z_2	Mean depth of lower boundary of seismically imaged pycnocline		m	L
$\langle \tan(\gamma) \rangle_p$	Mean slope of tracked reflections within pycnocline			Dimensionless

manuscript submitted to *JGR: Oceans*

©2020 American Geophysical Union. All rights reserved.

Accepted Article

Table 2. Table 1 continued.

Symbol	Description	Value	Unit	Dimension
Two-Layer System				
f	Coriolis parameter	1.29×10^{-4}	s^{-1}	T^{-1}
g	Gravitational acceleration	9.81	m s^{-2}	L T^{-2}
g'	Reduced gravity		m s^{-2}	L T^{-2}
L_R	Rossby radius of deformation	13	km	L
Turbulent Mixing				
$\hat{c}$	Intercept fitted to identified turbulent spectral subranges			Dimensionless
cpm	cycles per meter		cpm	L^{-1}
C_T	Obukhov-Corrsin constant	0.4		Dimensionless
K	Diapycnal (eddy) diffusivity		m^2 s^{-1}	L^2 T^{-1}
k_x	Component of horizontal wavenumber in plane of seismic image		cpm	L^{-1}
Γ	Turbulent flux coefficient	0.2		Dimensionless
ϵ	Dissipation rate of turbulent kinetic energy		m^2 s^{-3}	L^2 T^{-3}
$\phi_\xi(k_x)$	Power spectrum of vertical displacement		m^2 $[cpm]^{-1}$	L^3
$\phi_{\xi_x}(k_x)$	Power spectrum of horizontal gradient of vertical displacement		$[cpm]^{-1}$	L
$\langle \phi_{\xi_x} \rangle_p$	Mean ϕ_{ξ_x} within seismically imaged pycnocline		$[cpm]^{-1}$	L

manuscript submitted to *JGR: Oceans*

©2020 American Geophysical Union. All rights reserved.

Accepted Article

Table 3. Table 1 continued

Symbol	Description	Value	Unit	Dimension
Fitted Gaussian Vortex				
r	Radial distance from center of vortex		km	L
R_g	Core radius	$\sim$ 20–50	km	L
r_m	Radius of maximum azimuthal velocity	$\sim$ 14–35	km	L
u_t	Translational speed	$\sim$ 0.01–0.1	m s^{-1}	L T^{-1}
$u_\theta(r)$	Azimuthal velocity		m s^{-1}	L T^{-1}
u_{θ_m}	Maximum azimuthal velocity	$\sim$ 0.3–0.4	m s^{-1}	L T^{-1}
V_g	Length scale for azimuthal velocity	$\sim$ 1.4–1.9	m s^{-1}	L T^{-1}
Sea-Surface Heights				
h	Interface depth for 1-$\frac{1}{2}$-layer ocean		m	L
h_∞	Unperturbed interface depth for 1-$\frac{1}{2}$-layer ocean		m	L
$u_{sg_\perp}$	Cross-track component of geostrophic velocity		m s^{-1}	L T^{-1}
η	Sea-surface height anomaly		m	L
η_7	Smoothed sea-surface height anomaly		m	L

©2020 American Geophysical Union. All rights reserved.

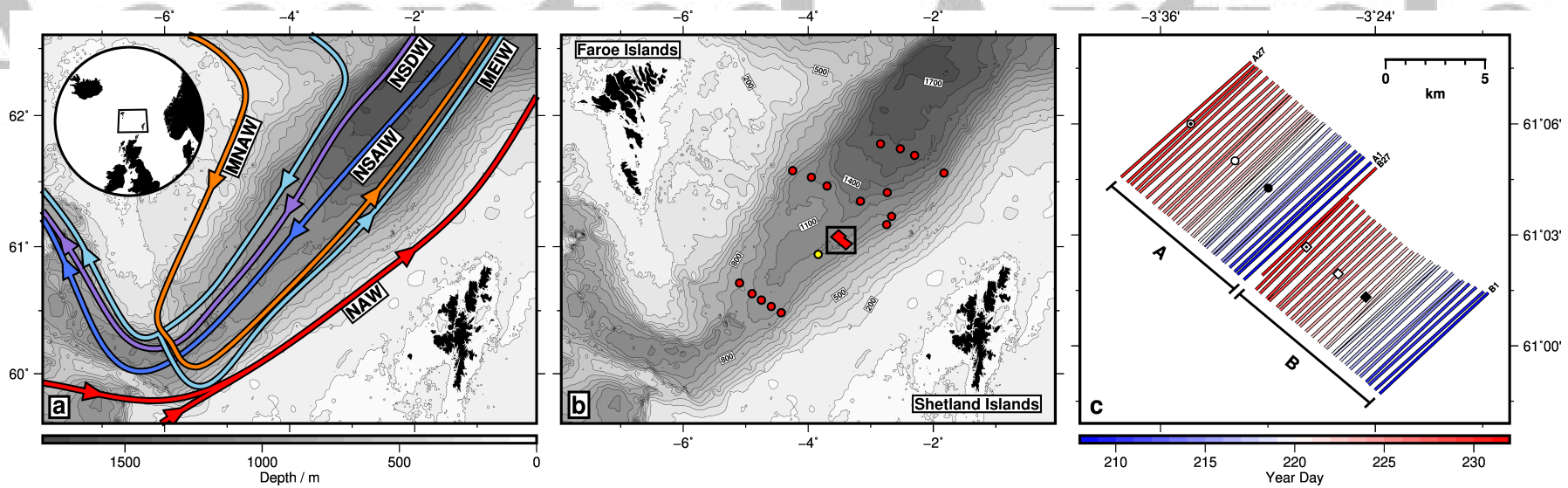

Figure 1. Location of 3D seismic survey. (a) Map of region including Faroe-Shetland Channel that shows principal water masses after McKenna et al. (2016). NSDW = Norwegian Sea Deep Water (purple); NSAIW = Norwegian Sea Arctic Intermediate Water (dark blue); MEIW = Modified East Icelandic Water (light blue); MNAW = Modified North Atlantic Water (orange); NAW = North Atlantic Water (red). Thin black lines = bathymetric contours at 100 m intervals (see panel (b) for labels). (b) Map that shows location of 3D seismic reflection survey. Red polygon = seismic survey generously made available by PGS ASA; black box = panel (c) of this figure; colored circles = locations of 26 CTD casts acquired in water depths > 800 m during June-September 1997 with repeated measurements in some cases; yellow circle = location of cast used to compute synthetic seismogram shown in Figure 2i. (c) Enlarged map showing geometry of 3D seismic acquisition. Colored lines = 54 ship transects according to Year Day of acquisition shown by scale bar (transects labeled A1–A27 within Sector A were acquired from southwest to northeast, transects labeled B1–B27 within Sector B were acquired from northeast to southwest); black/white circles indicate transects shown in Figure 3; black/white diamonds indicate transects shown in Figures 5 and 6.

©2020 American Geophysical Union. All rights reserved.

manuscript submitted to *JGR: Oceans*

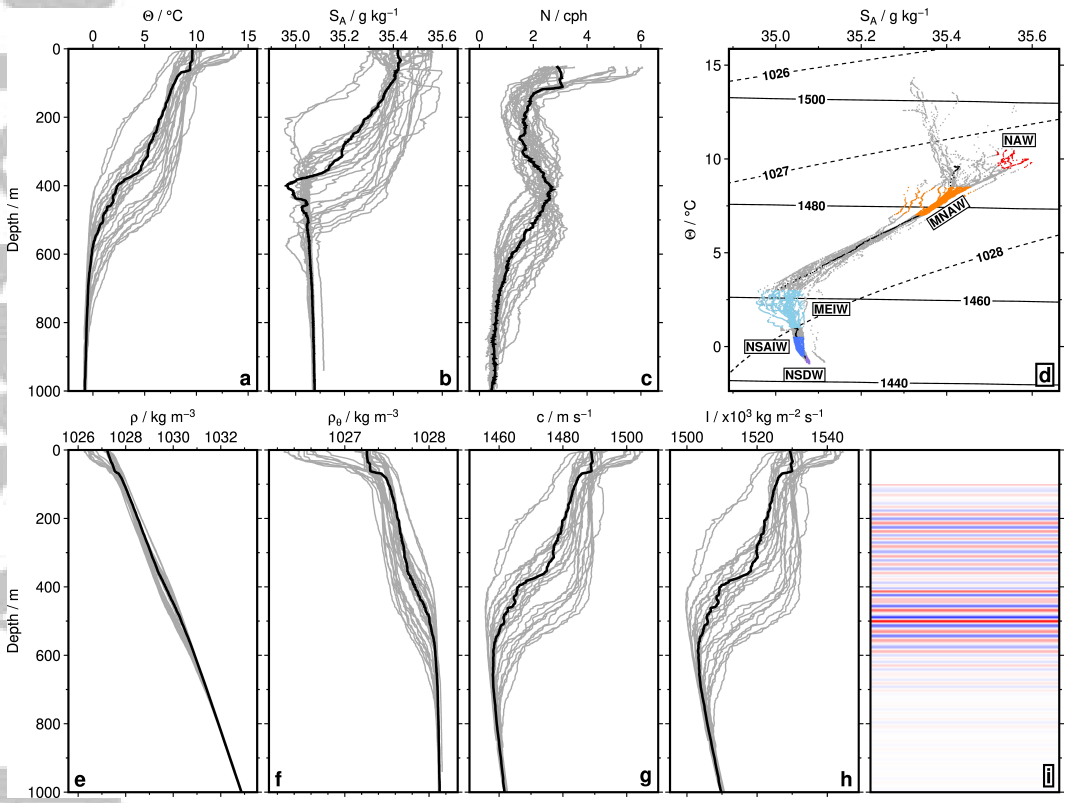

Figure 2. Hydrographic profiles from 26 CTD casts acquired during June-September 1997 (see Figure 1b for location). (a) Conservative temperature, Θ, plotted as function of depth. Black line = profile for CTD cast shown as yellow circle on Figure 1b that is used to compute synthetic seismogram shown in panel (i); gray lines = profiles for other CTD casts. (b) Absolute salinity, S_A, plotted as function of depth. (c) Buoyancy frequency, N, plotted as function of depth where profiles have been smoothed using boxcar filter with length of 100 m. cph = cycles per hour. (d) Θ–S_A diagram. NSDW = Norwegian Sea Deep Water (purple); NSAIW = Norwegian Sea Arctic Intermediate Water (dark blue); MEIW = Modified East Icelandic Water (light blue); MNAW = Modified North Atlantic Water (orange); NAW = North Atlantic Water (red). Water mass interpretation based on temperature and salinity ranges from Hansen and Østerhus (2000). (e) *in situ* density, ρ, as function of depth. (f) Potential density, ρ_θ, as function of depth. (g) Sound speed, c, as function of depth. (h) Acoustic impedance, I, as function of depth. (i) Synthetic seismogram computed from CTD cast highlighted by black line in panels (a)–(h). Red/blue stripes = positive/negative acoustic amplitudes.

©2020 American Geophysical Union. All rights reserved.

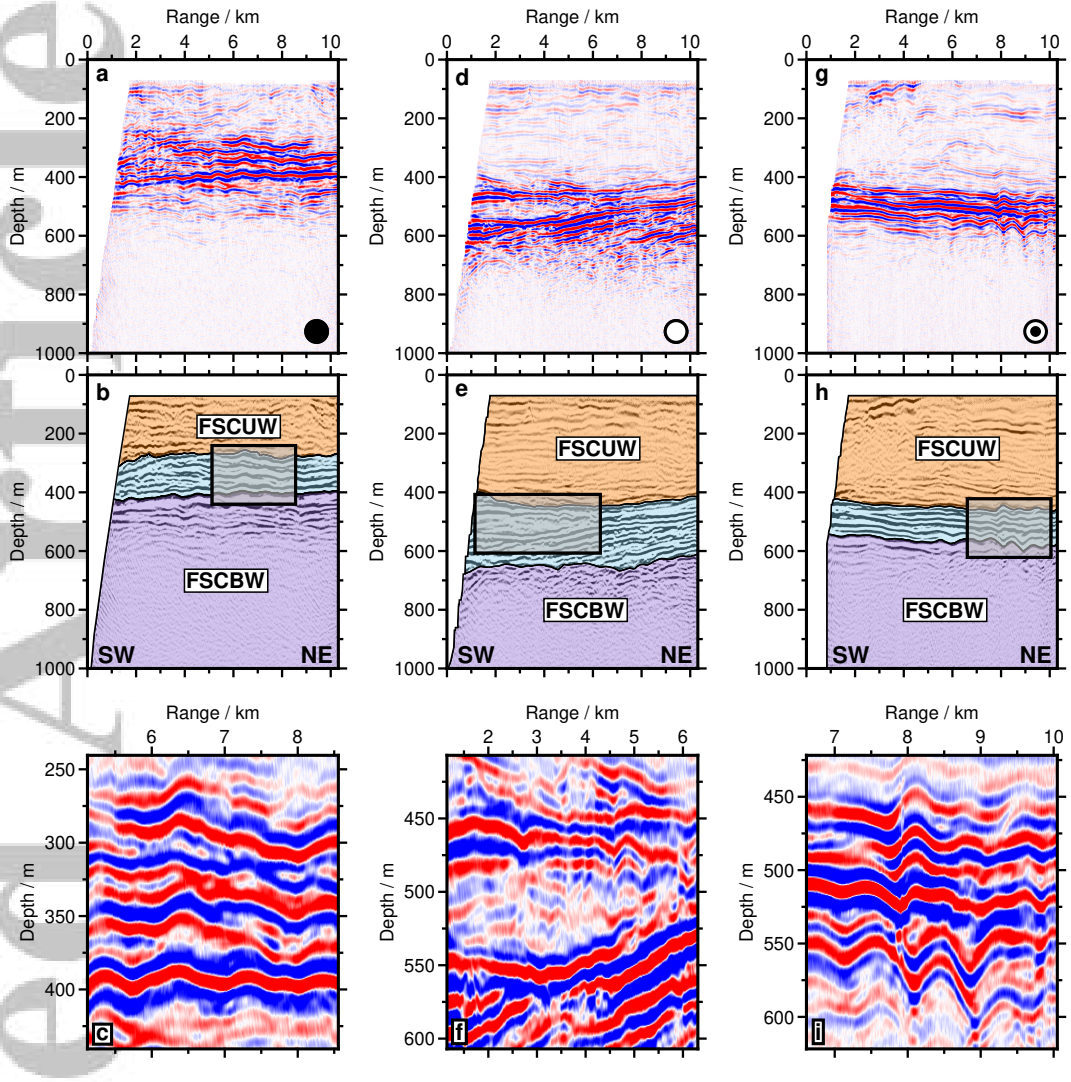

Figure 3. Water mass identification on seismic images. (a) Seismic image of transect A9 plotted as function of range and depth (see transect marked by black dot on Figure 1c for location). Red/blue stripes = positive/negative acoustic amplitudes. Vertical exaggeration is 10 times. Note that range is measured from most southwesterly point on images presented here and in later figures. (b) Qualitative hydrographic interpretation of panel (a). Yellow overlay = Faroe-Shetland Channel Upper Water (FSCUW); blue overlay = pycnocline; purple overlay = Faroe-Shetland Channel Bottom Water (FSCBW). Note that boundaries between water masses are more gradational than indicated here. Black box indicates location of panel (c). (c) Magnified portion of panel (b) that shows anastomosing internal waves. (d)–(f) Seismic image, interpretation and magnified portion of transect A17. Note internal waves and prominent submesoscale vortex within pycnocline. (g)–(i) Seismic image, interpretation and magnified portion of transect A26. Note spectacular non-linear internal waves with amplitudes of up to 30 m.

©2020 American Geophysical Union. All rights reserved.

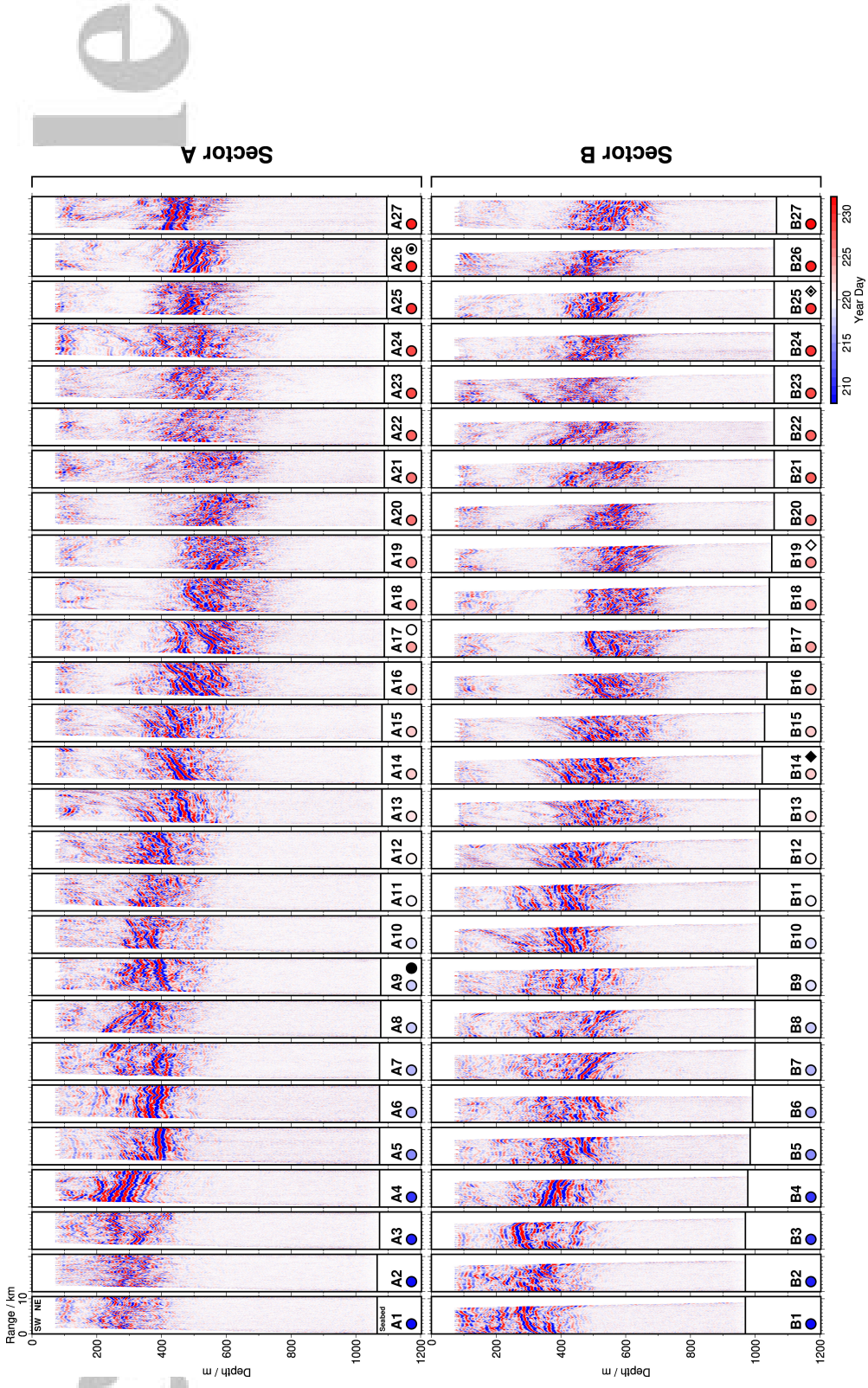

Figure 4. 54 seismic images from Sector A (upper row) and Sector B (lower row) plotted as functions of range and depth (see Figure 1c for location). Each image is labeled with transect number and oriented as shown for transect A1 at top left-hand side. Elapsed time increases from left to right along each row with colored circles indicating Year Day of acquisition according to scale bar at bottom right-hand side. Black/white circles indicate transects shown in Figure 3; black/white diamonds indicate transects shown in Figures 5 and 6. Vertical exaggeration is 100 times.

©2020 American Geophysical Union. All rights reserved.

Accepted Article

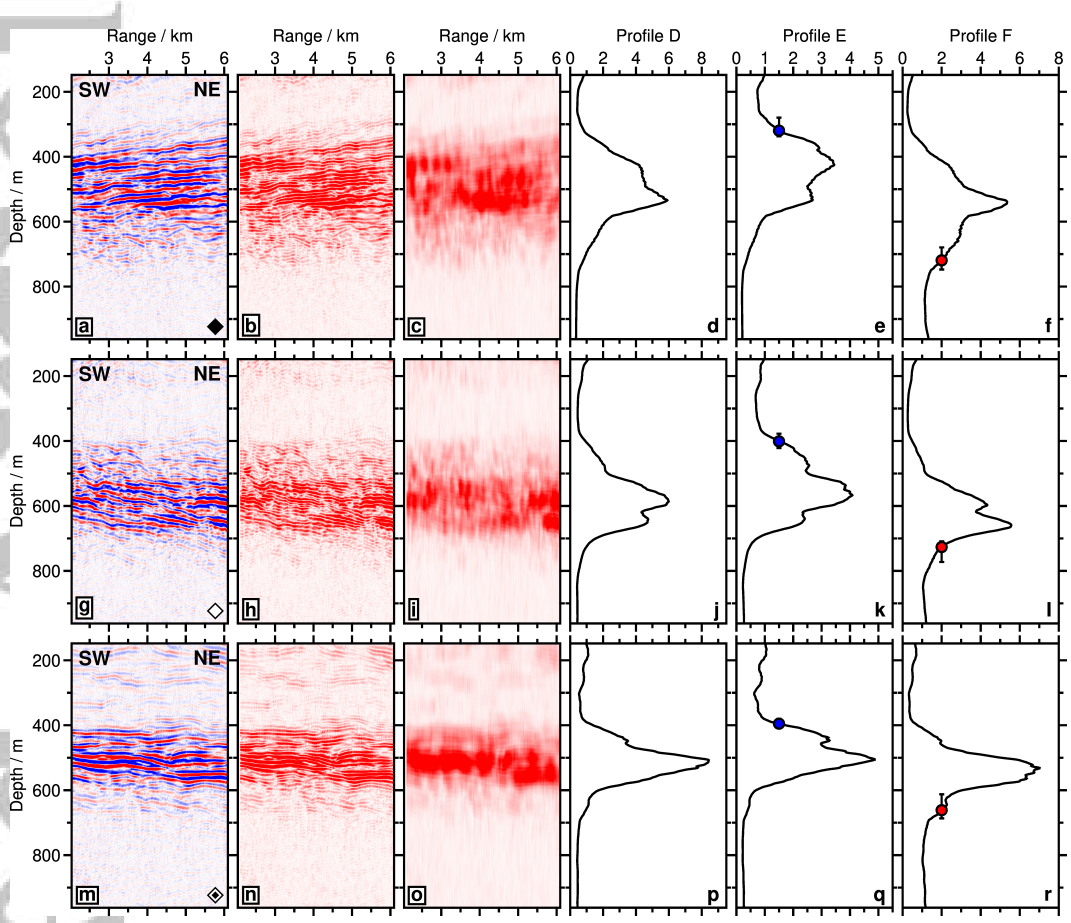

Figure 5. Identification of pycnocline. (a) Seismic image of transect B14 excluding outermost 1 km on each side (see transect indicated by black diamond on Figure 1c for location). (b) Same image that shows absolute seismic amplitudes. (c) Same image that shows vertically smoothed absolute amplitudes. (d) Horizontally averaged absolute amplitudes as function of depth calculated from panel (c). (e) Horizontally averaged absolute amplitudes as function of depth normalized by mean value of amplitudes at shallower depths. Blue circle with error bar = depth, z_1, of upper boundary of pycnocline. (f) Horizontally averaged absolute amplitudes as function of depth normalized by mean value of amplitudes at greater depths. Red circle with error bar = depth, z_2, of lower boundary of pycnocline. (g)–(l) Same for seismic image of transect B19. (m)–(r) Same for seismic image of transect B25.

©2020 American Geophysical Union. All rights reserved.

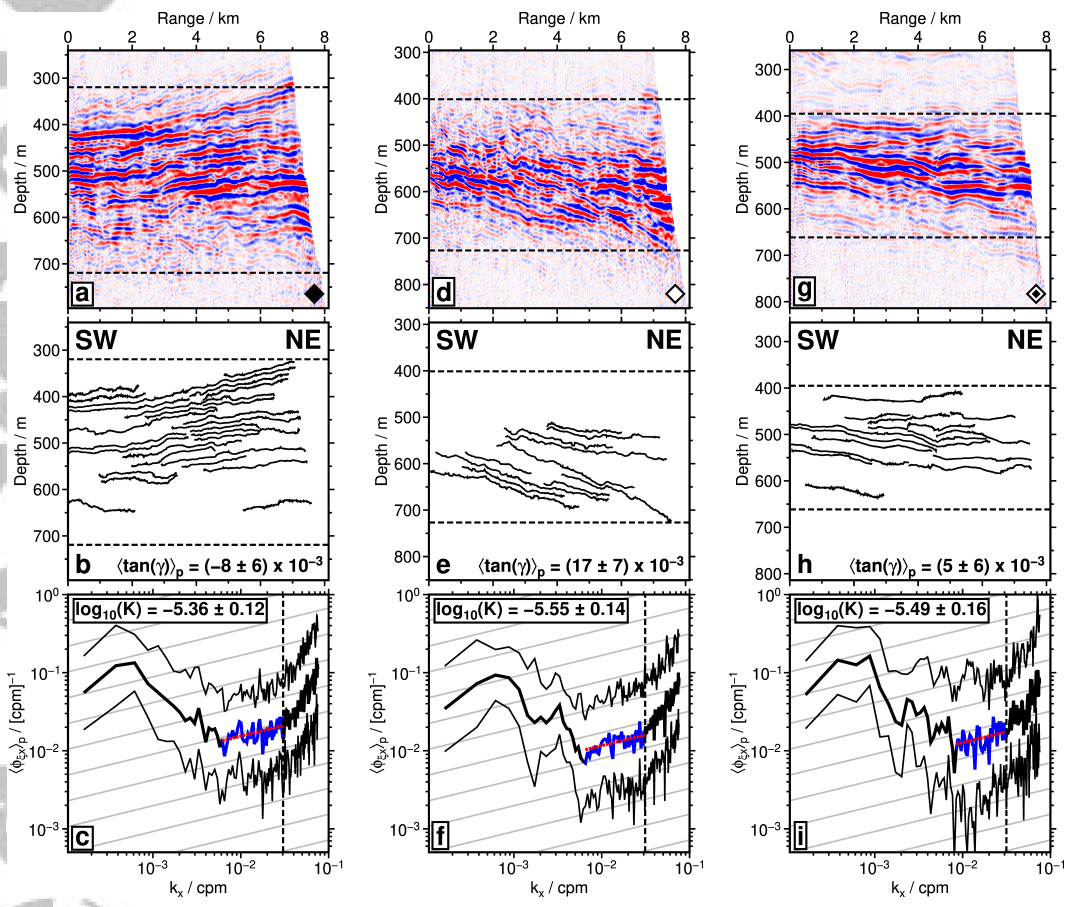

Figure 6. Estimation of tilt of reflections and of diapycnal diffusivity. (a) Seismic image of transect B14 (see transect marked by black diamond on Figure 1c for location). Pair of horizontal dashed lines demarcate upper boundary, z_1, and lower boundary, z_2, of identified pycnocline (see Figure 5). (b) Automatically tracked reflections on image, each of which is > 2 km in length, between depths of z_1 and z_2. Value of mean tilt, $\langle \tan(\gamma) \rangle_p$, is given at bottom right. (c) Mean power of horizontal gradient of vertical displacement of tracked reflections from panel (b), $\langle \phi_{\xi_x} \rangle_p$, as function of horizontal wavenumber, k_x. Thick/thin black lines = average values of $\langle \phi_{\xi_x} \rangle_p \pm 1\sigma$; blue line = identified turbulent subrange; dashed red line = fitted gradient of $+1/3$; gray reticule = gradient of $+1/3$; vertical dashed line = white noise cut-off. Estimated value of $\log_{10}(K)$ and its uncertainty shown in top left-hand corner. Note that this uncertainty only accounts for expected variation in buoyancy frequency and for error in straight line fitting. (d)–(f) Same for transect B19. (g)–(i) Same for transect B25.

©2020 American Geophysical Union. All rights reserved.

Accepted Article

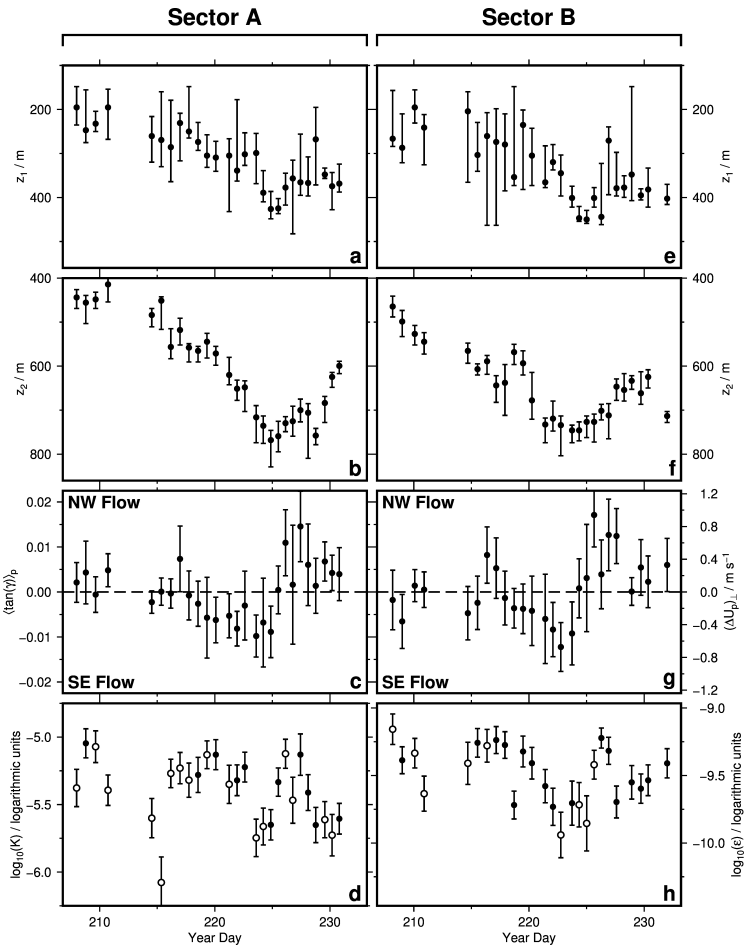

Figure 7. Temporal evolution of pycnoclinic depth, reflection tilt, and diapycnal diffusivity. (a) Depth, z_1, of upper boundary of seismically imaged pycnocline as function of time for 27 transects of Sector A. Solid circles and vertical bars = individual measurements and uncertainties obtained from amplitude analysis of each image. (b) Depth, z_2, of lower boundary of pycnocline as function of time for Sector A. (c) Mean gradient, $\langle\tan(\gamma)\rangle_p$, of tracked reflections $>$ 2 km long that lie between z_1 and z_2 as function of time for Sector A. Horizontal dashed line represents $\langle\tan(\gamma)\rangle_p = 0$; right-hand y-axis shows calculated change in out-of-plane component of geostrophic velocity, $(\Delta U_p)_\perp$, across pycnocline with labeled direction of flow; vertical bars = standard deviation of $\langle\tan(\gamma)\rangle_p$. (d) Diapycnal diffusivity, K, as function of time for Sector A. Black circles and vertical bars = $\log_{10}(K) \pm 1\sigma$ estimated from identified turbulent subranges that have gradient of $+1/3 \pm 0.3$; open circles and vertical bars = $\log_{10}(K) \pm 1\sigma$ estimated from other turbulent subranges; right-hand y-axis shows equivalent values of turbulent dissipation rate, ϵ. Note that uncertainty for $\log_{10}(K)$ only accounts for expected variation in buoyancy frequency and for errors in straight line fitting. (e)–(h) Same for 27 transects of Sector B.

©2020 American Geophysical Union. All rights reserved.

Accepted Article

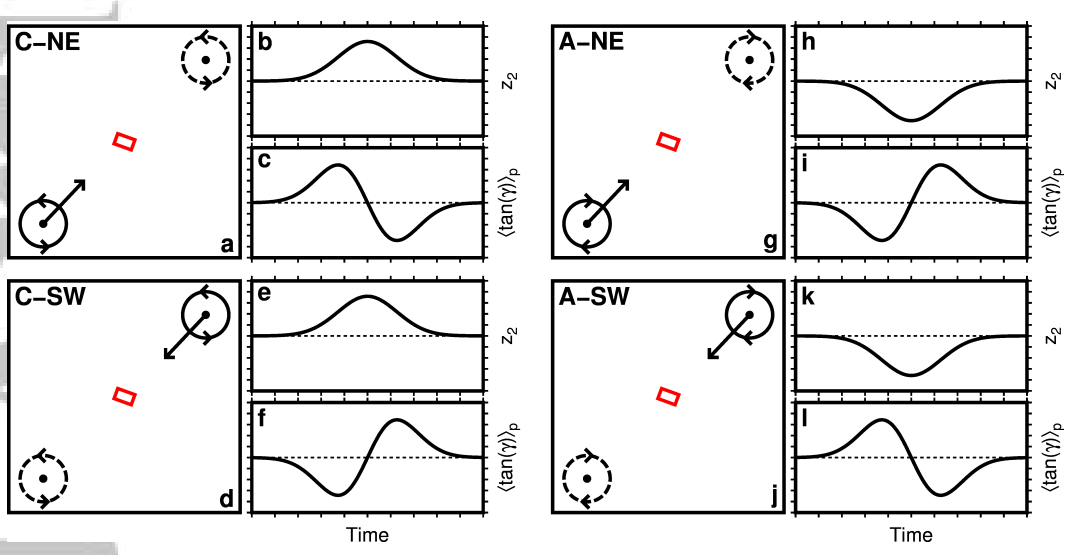

Figure 8. Cartoons that show expected changes in pycnoclinic depth, z_2, and reflection tilt, $\langle\tan(\gamma)\rangle_p$, for cyclonic and anticyclonic vortices that translate along channel. Note that diagrams are not to scale. (a) Plan view of cyclonic vortex translating northeastward (C-NE). Solid circle with arrows = vortex at initial time; dashed circle with arrows = vortex at final time; red box = locus of seismic survey. (b) Solid line = expected change of z_2 as function of time; dashed line = unperturbed pycnoclinic depth. (c) Solid line = expected change of $\langle\tan(\gamma)\rangle_p$ as function of time; dashed line shows $\langle\tan(\gamma)\rangle_p = 0$; $\langle\tan(\gamma)\rangle_p < 0$ corresponds to southeastward flow; $\langle\tan(\gamma)\rangle_p > 0$ corresponds to northwestward flow. (d)–(f) Cyclonic vortex that translates southwestward (C-NE). (g)–(i) Anticyclonic vortex that translates northeastward (A-NE). (j)–(l) Anticyclonic vortex that translates southwestward (A-SW).

©2020 American Geophysical Union. All rights reserved.

Accepted Article

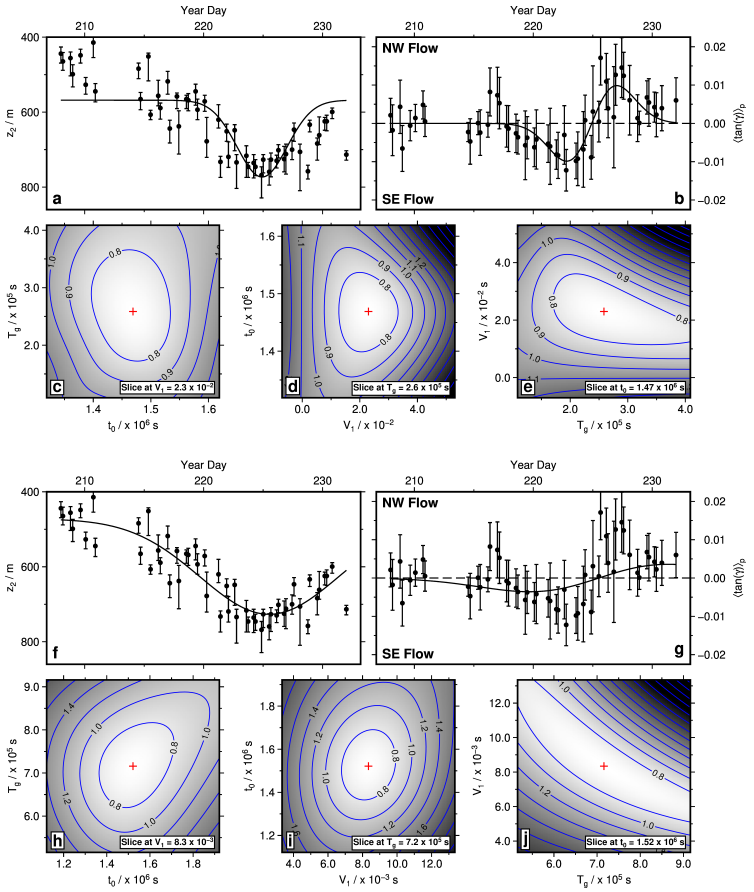

Figure 9. Calculations for optimal vortical geometry by fitting values of pycnoclinic depth, z_2, and mean reflection tilt, $\langle \tan(\gamma) \rangle_p$. (a) Solid circles with vertical bars = values of z_2 and their uncertainties as function of time; solid line = best-fitting relationship for model fitted to $\langle \tan(\gamma) \rangle_p$ (see Equation (17)). (b) Solid circles with vertical bars = values of $\langle \tan(\gamma) \rangle_p$ and their uncertainties as function of time; solid line = best-fitting relationship; dashed line shows $\langle \tan(\gamma) \rangle_p = 0$. (c) Misfit between observed and calculated values of $\langle \tan(\gamma) \rangle_p$ plotted as function of T_g and t_0 for given value of V_1. Red cross = locus of global minimum. (d) Same as function of t_0 and V_1 for given value of T_g. (e) Same as function of V_1 and T_g for given value of t_0. (f) Solid circles with vertical bars = values of z_2 as function of time; solid line = best-fitting relationship (see Equation (18)). (g) Solid circles with vertical bars = values of $\langle \tan(\gamma) \rangle_p$ as function of time; solid line = best-fitting relationship for model fitted to z_2; dashed line shows $\langle \tan(\gamma) \rangle_p = 0$. (h) Misfit between observed and calculated values of z_2 plotted as function of T_g and t_0 for given value of V_1. Red cross = locus of global minimum. (i) Same as function of t_0 and V_1 for given value of T_g. (j) Same as function of V_1 and T_g for given value of t_0.

©2020 American Geophysical Union. All rights reserved.

Accepted Article

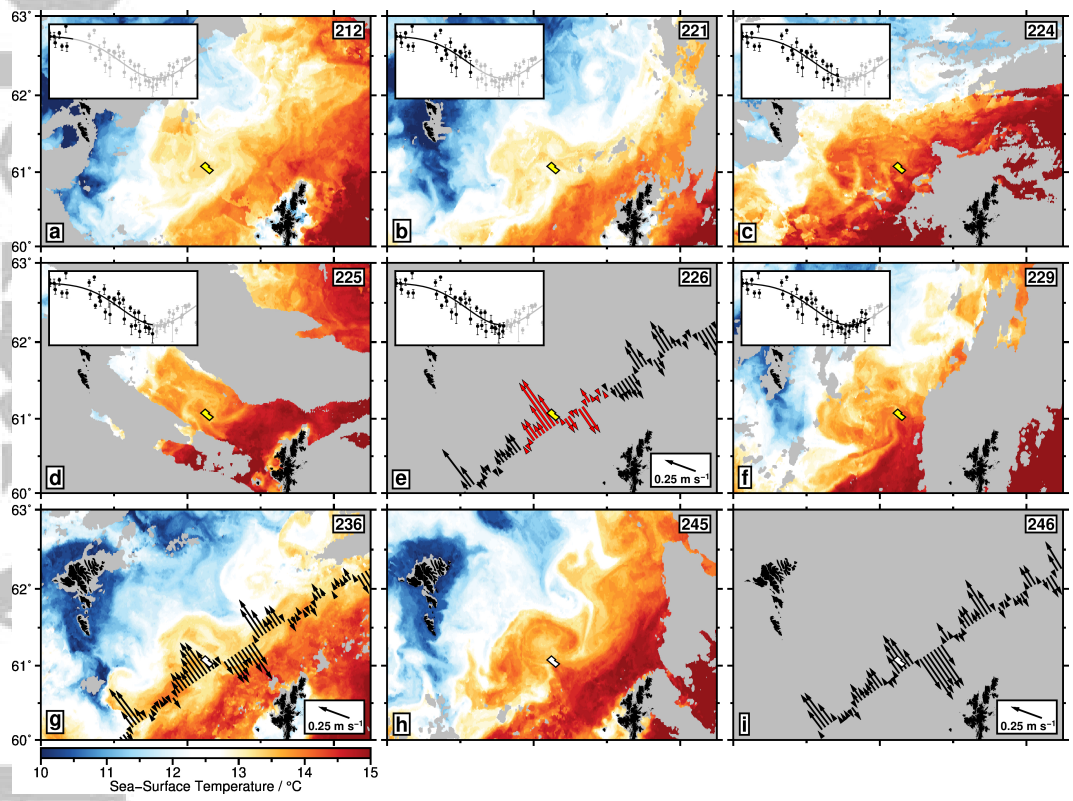

Figure 10. Sea-surface temperature and geostrophic current measurements. (a) Satellite image of sea-surface temperature for Year Day 212. Blue/white/red colors = sea-surface temperature variation calculated from $\lesssim$ 8 individual passes of AVHRR satellite over course of single day (see scale bar at bottom left-hand side); gray polygons = regions obscured by cloud; black polygons = land; yellow box with black outline = locus of seismic survey where color indicates coincident seismic acquisition; inset panel shows set of seismically derived z_2 measurements where black circles/line = values up to and including Year Day 212; gray circles/line = future values). (b)–(d) Same for Year Days 221, 224 and 225. (e) Same for Year Day 226. Transect with black/red arrows = cross-track geostrophic velocity component estimated from sea-surface altimetric data acquired by single pass of TOPEX/Poseidon satellite (red arrows denote measurements used in Figure 11). Note scale at bottom right-hand side. (f) Same for Year Day 229. (g)–(i) Same for Year Days 236, 245 and 246. Gray box with black outline = locus of seismic survey where color indicates point in time when seismic acquisition ended. Satellite images courtesy of NEODAAS; altimetric records courtesy of RADS.

©2020 American Geophysical Union. All rights reserved.

Accepted Article

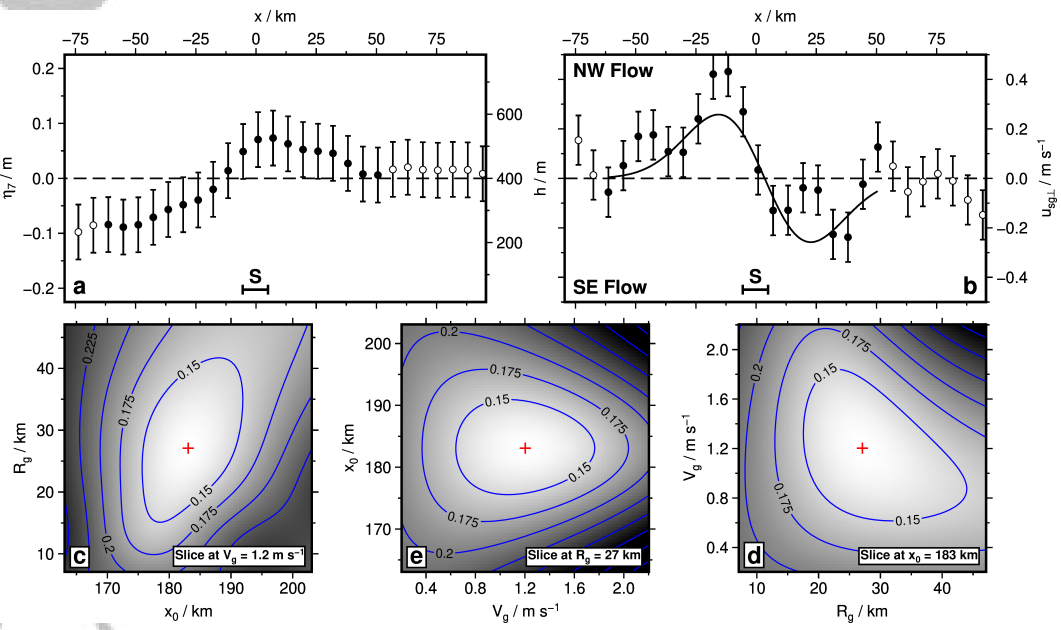

Figure 11. Sea-surface height anomalies and cross-track geostrophic velocity measurements. (a) Black/open circles and vertical bars = selected smoothed sea-surface height anomalies, η_7, and associated uncertainties as function of along-track distance, x, for Year Day 226 (measurements are colocated with red arrows shown in 10f); dashed horizontal line = 0 m; horizontal bar labeled S = approximate locus of seismic survey at $x = 0$ km. (b) Black/open circles and vertical bars = corresponding cross-track altimetric geostrophic velocities, $u_{sg_\perp}$, and associated uncertainties as function of x that show anticyclonic flow; black line = best-fitting relationship (see Equation (20)); dashed horizontal line = 0 m s^{-1}; $u_{sg_\perp} < 0$ m s^{-1} = northwestward flow; $u_{sg_\perp} > 0$ m s^{-1} = southeastward flow. (c)–(e) Slices through misfit function as function of R_g, x_0 and V_g. Red cross = locus of global minimum.

©2020 American Geophysical Union. All rights reserved.

References

Apel, J. R. (Ed.). (1972). *Sea surface topography from space: Proceedings.* Environmental Research Laboratories, National Oceanic and Atmospheric Administration, US Department of Commerce.

Baker, M. A., & Gibson, C. H. (1987). Sampling turbulence in the stratified ocean: Statistical consequences of strong intermittency. *Journal of Physical Oceanography*, *17*(10), 1817–1836. doi: 10.1175/1520-0485(1987)017⟨1817:STITSO⟩2.0.CO;2

Barbosa Aguiar, A. C., Ménesguen, C., Le Gentil, S., Schopp, R., & Carton, X. (2015). Cyclones and anticyclones in seismic imaging. *Journal of Physical Oceanography*, *45*(9), 2436-2443. doi: 10.1175/JPO-D-15-0066.1

Barnes, A. E. (2007). A tutorial on complex seismic trace analysis. *Geophysics*, *72*(6), W33–W43. doi: 10.1190/1.2785048

Berx, B., Hansen, B., Østerhus, S., Larsen, K. M., Sherwin, T. J., & Jochumsen, K. (2013). Combining in situ measurements and altimetry to estimate volume, heat and salt transport variability through the Faroe-Shetland Channel. *Ocean Science*, *9*(4), 639–654. doi: 10.5194/os-9-639-2013

Biescas, B., Ruddick, B. R., Nedimovic, M. R., Sallarès, V., Bornstein, G., & Mojica, J. F. (2014). Recovery of temperature, salinity, and potential density from ocean reflectivity. *Journal of Geophysical Research: Oceans*, *119*(5), 3171–3184. doi: 10.1002/2013JC009662

Blacic, T. M., & Holbrook, W. S. (2010). First images and orientation of fine structure from a 3-D seismic oceanography data set. *Ocean Science*, *6*(2), 431–439. doi: 10.5194/os-6-431-2010

Booth, D. A., & Ellett, D. (1983). The Scottish continental slope current. *Continental Shelf Research*, *2*(2), 127–146. doi: 10.1016/0278-4343(83)90012-2

Broadbridge, M. B., & Toumi, R. (2015). The deep circulation of the Faroe-Shetland Channel: Opposing flows and topographic eddies. *Journal of Geophysical Research: Oceans*, *120*(9), 5983–5996. doi: 10.1002/2015JC010833

Buchholtz, H. (1972). A note on signal distortion due to dynamic (NMO) corrections. *Geophysical Prospecting*, *20*(2), 395–402. doi: 10.1111/j.1365-2478.1972.tb00642.x

Carton, X. (2001). Hydrodynamical modeling of oceanic vortices. *Surveys in Geo-*

©2020 American Geophysical Union. All rights reserved.

physics, *22*(3), 179–263. doi: 10.1023/A:1013779219578

Carton, X., Flierl, G., & Polvani, L. (1989). The generation of tripoles from unstable axisymmetric isolated vortex structures. *EPL (Europhysics Letters)*, *9*(4), 339–334. doi: 10.1209/0295-5075/9/4/007

Chafik, L. (2012). The response of the circulation in the Faroe-Shetland Channel to the North Atlantic Oscillation. *Tellus A: Dynamic Meteorology and Oceanography*, *64*(1), 18423. doi: 10.3402/tellusa.v64i0.18423

Cushman-Roisin, B., & Merchant-Both, S. (1995). Elliptical warm-core rings in a two-layer ocean with ambient shear. *Journal of Physical Oceanography*, *25*(9), 2011–2024. doi: 10.1175/1520-0485(1995)025⟨2011:EWCRIA⟩2.0.CO;2

Darelius, E., Ullgren, J. E., & Fer, I. (2013). Observations of barotropic oscillations and their influence on mixing in the Faroe Bank Channel overflow region. *Journal of Physical Oceanography*, *43*(7), 1525–1532. doi: 10.1175/JPO-D-13-059.1

D'Asaro, E. A., & Lien, R.-C. (2000). The wave-turbulence transition for stratified flows. *Journal of Physical Oceanography*, *30*(7), 1669–1678. doi: 10.1175/1520-0485(2000)030⟨1669:TWTTFS⟩2.0.CO;2

Dickinson, A., White, N. J., & Caulfield, C. P. (2017). Spatial variation of diapycnal diffusivity estimated from seismic imaging of internal wave field, Gulf of Mexico. *Journal of Geophysical Research: Oceans*, *122*(12), 9827–9854. doi: 10.1002/2017JC013352

Dooley, H. (1975). Features of hydrography and currents in the Faroe-Shetland Channel during Overflow '73. *Rep. CM*, *100*, 31.

Dooley, H. D., & Meincke, J. (1981). Circulation and water masses in the Faroese Channels during Overflow '73. *Deutsche Hydrografische Zeitschrift*, *34*(2), 41–55. doi: 10.1007/BF02226585

Falder, M., White, N. J., & Caulfield, C. P. (2016). Seismic imaging of rapid onset of stratified turbulence in the South Atlantic Ocean. *Journal of Physical Oceanography*, *46*(4), 1023–1044. doi: 10.1175/JPO-D-15-0140.1

Ferrari, R. (2014). What goes down must come up. *Nature*, *513*(7517), 179–180. doi: 10.1038/513179a

Ferrari, R., & Wunsch, C. (2009). Ocean circulation kinetic energy: Reservoirs, sources, and sinks. *Annual Review of Fluid Mechanics*, *41*(1), 253–282. doi: 10

©2020 American Geophysical Union. All rights reserved.

.1146/annurev.fluid.40.111406.102139

Ferrari, R., & Wunsch, C. (2010). The distribution of eddy kinetic and potential energies in the global ocean. *Tellus A: Dynamic Meteorology and Oceanography*, *62*(2), 92–108. doi: 10.1111/j.1600-0870.2009.00432.x

Gallego, A., Murray, R. O., Berx, B., Turrell, W. R., Beegle-Krause, C., Inall, M., ... Mulanaphy, N. (2018). Current status of deepwater oil spill modelling in the Faroe-Shetland Channel, Northeast Atlantic, and future challenges. *Marine Pollution Bulletin*, *127*, 484–504. doi: 10.1016/j.marpolbul.2017.12.002

Garrett, C., & Munk, W. (1972). Space-Time Scales of Internal Waves. *Geophysical Fluid Dynamics*, *2*(1), 225–264. doi: 10.1080/03091927208236082

Gerkema, T. (1996). A unified model for the generation and fission of internal tides in a rotating ocean. *Journal of Marine Research*, *54*(3), 421–450. doi: 10.1357/0022240963213574

Gould, W., Loynes, J., & Backhaus, J. (1985). Seasonality in slope current transports N.W. of Shetland. *ICES CM*, *100*, 7.

Gregg, M. C. (1980). Microstructure patches in the thermocline. *Journal of Physical Oceanography*, *10*(6), 915–943. doi: 10.1175/1520-0485(1980)010⟨0915:MPITT⟩2.0.CO;2

Gregg, M. C. (1987). Diapycnal mixing in the thermocline: A review. *Journal of Geophysical Research: Oceans*, *92*(C5), 5249–5286. doi: 10.1029/JC092iC05p05249

Gregg, M. C., & Cox, C. S. (1971). Measurements of the oceanic microstructure of temperature and electrical conductivity. *Deep Sea Research and Oceanographic Abstracts*, *18*(9), 925–934. doi: 10.1016/0011-7471(71)90067-2

Gregg, M. C., Seim, H. E., & Percival, D. B. (1993). Statistics of shear and turbulent dissipation profiles in random internal wave fields. *Journal of Physical Oceanography*, *23*(8), 1777–1799. doi: 10.1175/1520-0485(1993)023⟨1777:SOSATD⟩2.0.CO;2

Griffiths, R., & Hopfinger, E. (1987). Coalescing of geostrophic vortices. *Journal of Fluid Mechanics*, *178*, 73–97. doi: 10.1017/S0022112087001125

Hall, R. A., Berx, B., & Damerell, G. M. (2019). Internal tide energy flux over a ridge measured by a co-located ocean glider and moored acoustic Doppler current profiler. *Ocean Science*, *15*(6), 1439–1453. doi: 10.5194/os-15-1439-2019

©2020 American Geophysical Union. All rights reserved.

Hall, R. A., Huthnance, J. M., & Williams, R. G. (2011). Internal tides, nonlinear internal wave trains, and mixing in the Faroe-Shetland Channel. *Journal of Geophysical Research: Oceans*, *116*(C3). doi: 10.1029/2010JC006213

Hansen, B., & Jákupsstovu, S. (1995). Blue whiting post-spawning migration: Is it determined by the flow field? *Ocean Challenge*, *6*, 36–39.

Hansen, B., & Jákupsstovu, S. H. (1992). Availability of blue whiting (*Micromesistius poutassou*) in Faroese waters in relation to hydrography. *ICES Marine Science Symposia*, *195*, 349–360.

Hansen, B., & Meincke, J. (1979). Eddies and meanders in the Iceland-Faroe Ridge area. *Deep Sea Research Part A. Oceanographic Research Papers*, *26*(9), 1067–1082. doi: 10.1016/0198-0149(79)90048-7

Hansen, B., & Østerhus, S. (2000). North Atlantic-Nordic Seas exchanges. *Progress in Oceanography*, *45*(2), 109–208. doi: 10.1016/S0079-6611(99)00052-X

Holbrook, W. S., Fer, I., Schmitt, R. W., Lizarralde, D., Klymak, J. M., Helfrich, L. C., & Kubichek, R. (2013). Estimating Oceanic Turbulence Dissipation from Seismic Images. *Journal of Atmospheric and Oceanic Technology*, *30*(8), 1767–1788. doi: 10.1175/JTECH-D-12-00140.1

Holbrook, W. S., Páramo, P., Pearse, S., & Schmitt, R. W. (2003). Thermohaline Fine Structure in an Oceanographic Front from Seismic Reflection Profiling. *Science*, *301*(5634), 821–824. doi: 10.1126/science.1085116

Hopfinger, E. J., & van Heijst, G. J. F. (1993). Vortices in rotating fluids. *Annual Review of Fluid Mechanics*, *25*(1), 241–289. doi: 10.1146/annurev.fl.25.010193.001325

Hosegood, P., Bonnin, J., & van Haren, H. (2004). Solibore-induced sediment resuspension in the Faeroe-Shetland Channel. *Geophysical Research Letters*, *31*(9). doi: 10.1029/2004GL019544

IOC, SCOR, & IAPSO. (2010). The international thermodynamic equation of seawater — 2010: calculation and use of thermodynamic properties. *Intergovernmental Oceanographic Commission*, *56*, 196 pp.

Jacobsen, A. (1948). An instrument for recording continuously the salinity, temperature, and depth of sea water. *Transactions of the American Institute of Electrical Engineers*, *67*, 714–722.

Keogh, S., Robinson, I., Donlon, C., & Nightingale, T. (1999). The accuracy of

©2020 American Geophysical Union. All rights reserved.

AVHRR SST determined using shipborne radiometers. *International Journal of Remote Sensing*, *20*(14), 2871–2876. doi: 10.1080/014311699211840

Klaeschen, D., Hobbs, R. W., Krahmann, G., Papenberg, C., & Vsemirnova, E. (2009). Estimating movement of reflectors in the water column using seismic oceanography. *Geophysical Research Letters*, *36*(24). doi: 10.1029/2009GL038973

Klymak, J. M., & Moum, J. N. (2007a). Oceanic isopycnal slope spectra. Part I: Internal waves. *Journal of Physical Oceanography*, *37*(5), 1215–1231. doi: 10.1175/JPO3073.1

Klymak, J. M., & Moum, J. N. (2007b). Oceanic isopycnal slope spectra. Part II: Turbulence. *Journal of Physical Oceanography*, *37*(5), 1232–1245. doi: 10.1175/JPO3074.1

Knudsen, M. (1911). Danish hydrographical investigations at the Faroe Islands in the spring of 1910. *Meddelelser fra Kommissionen for Havundersogelser. Serie: Hydrografi*(11).

Komatitsch, D., & Tromp, J. (1999). Introduction to the spectral element method for three-dimensional seismic wave propagation. *Geophysical Journal International*, *139*(3), 806–822. doi: 10.1046/j.1365-246x.1999.00967.x

Krahmann, G., Papenberg, C., Brandt, P., & Vogt, M. (2009). Evaluation of seismic reflector slopes with a Yoyo-CTD. *Geophysical Research Letters*, *36*(24). (L00D02) doi: 10.1029/2009GL038964

Larsen, K. M. H., Hansen, B., Kristiansen, R., & Østerhus, S. (2000). Internal tides in the waters surrounding the Faroe Plateau. *ICES CM*, *50*, 9–13.

Leben, R. R., & Powell, B. S. (2003). Accuracy assessment of Jason-1 and TOPEX/POSEIDON along-track sea surface slope special issue: Jason-1 calibration/validation. *Marine Geodesy*, *26*(3-4), 355–366. doi: 10.1080/714044526

Lilly, J. M., Rhines, P. B., Schott, F., Lavender, K., Lazier, J., Send, U., & D'Asaro, E. (2003). Observations of the Labrador Sea eddy field. *Progress in Oceanography*, *59*(1), 75–176. doi: 10.1016/j.pocean.2003.08.013

Liu, Z., Lian, Q., Zhang, F., Wang, L., Li, M., Bai, X., ... Wang, F. (2017). Weak thermocline mixing in the North Pacific low-latitude western boundary current system. *Geophysical Research Letters*, *44*(20), 10–530. doi:

©2020 American Geophysical Union. All rights reserved.

10.1002/2017GL075210

Mashayek, A., Salehipour, H., Bouffard, D., Caulfield, C. P., Ferrari, R., Nikurashin, M., ... Smyth, W. D. (n.d.). Efficiency of turbulent mixing in the abyssal ocean circulation. *Geophysical Research Letters*, *44*(12), 6296–6306. doi: 10.1002/2016GL072452

McDougall, T. J. (1988). Neutral-surface potential vorticity. *Progress in Oceanography*, *20*(3), 185–221. doi: 10.1016/0079-6611(88)90002-X

McKenna, C., Berx, B., & Austin, W. E. N. (2016). The decomposition of the Faroe-Shetland Channel water masses using parametric optimum multi-parameter analysis. *Deep Sea Research Part I: Oceanographic Research Papers*, *107*, 9–21. doi: 10.1016/j.dsr.2015.10.013

McWilliams, J. C. (2016). Submesoscale currents in the ocean. *Proceedings of the Royal Society A: Mathematical, Physical and Engineering Sciences*, *472*(2189), 20160117. doi: 10.1098/rspa.2016.0117

Meincke, J., & Kvinge, T. (1978). On the atmospheric forcing of overflow events. *ICES. CM C*, *9*.

Meunier, T., Sanz, E. P., Tenreiro, M., Ochoa, J., Angulo, A. R., & Buckingham, C. (2019). Observations of layering under a warm-core ring in the Gulf of Mexico. *Journal of Physical Oceanography*, *49*(12), 3145–3162. doi: 10.1175/JPO-D-18-0138.1

Montgomery, R. B. (1939). Ein Versuch, den vertikalen und seitlichen Austausch in der Tiefe der Sprungschicht im äquatorialen Atlantischen Ozean zu bestimmen. *Annalen der Hydrographie und maritimen Meteorologie*, *67*, 242–246.

Munk, W. H. (1966). Abyssal recipes. *Deep Sea Research and Oceanographic Abstracts*, *13*(4), 707–730. doi: 10.1016/0011-7471(66)90602-4

Naeije, M., Doornbos, E., Mathers, L., Scharroo, R., Schrama, E., & Visser, P. (2002). Radar altimeter database system: Exploitation and extension (RADSxx). *Final Report, NUSP-2 Report*.

Nandi, P., Holbrook, W. S., Pearse, S., Páramo, P., & Schmitt, R. W. (2004). Seismic reflection imaging of water mass boundaries in the Norwegian Sea. *Geophysical Research Letters*, *31*(23). (L23311) doi: 10.1029/2004GL021325

Oey, L.-Y. (1997). Eddy energetics in the Faroe-Shetland channel: a model resolution study. *Continental Shelf Research*, *17*(15), 1929–1944. doi: 10.1016/S0278

©2020 American Geophysical Union. All rights reserved.

-4343(97)00053-8

Olsen, S. M., Hansen, B., Quadfasel, D., & Østerhus, S. (2008). Observed and modelled stability of overflow across the Greenland-Scotland ridge. *Nature*, *455*(7212), 519–522. doi: 10.1038/nature07302

Olson, D. B. (1980). The physical oceanography of two rings observed by the cyclonic ring experiment. Part II: Dynamics. *Journal of Physical Oceanography*, *10*(4), 514–528. doi: 10.1175/1520-0485(1980)010⟨0514:TPOOTR⟩2.0.CO;2

Olson, D. B. (1991). Rings in the ocean. *Annual Review of Earth and Planetary Sciences*, *19*(1), 283–311. doi: 10.1146/annurev.ea.19.050191.001435

Olson, D. B., Schmitt, R. W., Kennelly, M., & Joyce, T. M. (1985). A two-layer diagnostic model of the long-term physical evolution of warm-core ring 82B. *Journal of Geophysical Research: Oceans*, *90*(C5), 8813–8822. doi: 10.1029/JC090iC05p08813

Osborn, T. (1980). Estimates of the local rate of vertical diffusion from dissipation measurements. *Journal of Physical Oceanography*, *10*(1), 83–89. doi: 10.1175/1520-0485(1980)010⟨0083:EOTLRO⟩2.0.CO;2

Østerhus, S., Woodgate, R., Valdimarsson, H., Turrell, B., de Steur, L., Quadfasel, D., ... Berx, B. (2019). Arctic Mediterranean exchanges: a consistent volume budget and trends in transports from two decades of observations. *Ocean Science*, *15*(2), 379–399. doi: 10.5194/os-15-379-2019

Park, K.-A., Lee, E.-Y., Li, X., Chung, S.-R., Sohn, E.-H., & Hong, S. (2015). NOAA/AVHRR sea surface temperature accuracy in the East/Japan Sea. *International Journal of Digital Earth*, *8*(10), 784–804. doi: 10.1080/17538947.2014.937363

Pearse, S., Holbrook, W., Paramo, P., & Schmitt, R. (2003). Time-Lapse Seismic-Reflection Images Of Thermohaline Intrusions in an Oceanographic Front. In *AGU Fall Meeting Abstracts.*

Powell, B. S., & Leben, R. R. (2004). An optimal filter for geostrophic mesoscale currents from along-track satellite altimetry. *Journal of Atmospheric and Oceanic Technology*, *21*(10), 1633–1642. doi: 10.1175/1520-0426(2004)021⟨1633:AOFFGM⟩2.0.CO;2

Powell, M. J. D. (1964). An efficient method for finding the minimum of a function of several variables without calculating derivatives. *The Computer Jour-*

©2020 American Geophysical Union. All rights reserved.

nal, *7*(2), 155–162. doi: 10.1093/comjnl/7.2.155

Riley, J. J., & Lindborg, E. (2008). Stratified turbulence: A possible interpretation of some geophysical turbulence measurements. *Journal of the Atmospheric Sciences*, *65*(7), 2416–2424. doi: 10.1175/2007JAS2455.1

Rubino, A., Brandt, P., & Hessner, K. (1998). Analytical solutions for circular eddies of the reduced-gravity, shallow-water equations. *Journal of Physical Oceanography*, *28*(5), 999–1002. doi: 10.1175/1520-0485(1998)028⟨0999:ASFCEO⟩2.0.CO;2

Ruddick, B., Anis, A., & Thompson, K. (2000). Maximum likelihood spectral fitting: The Batchelor spectrum. *Journal of Atmospheric and Oceanic Technology*, *17*(11), 1541–1555. doi: 10.1175/1520-0426(2000)017⟨1541:MLSFTB⟩2.0.CO;2

Ruddick, B., Song, H., Dong, C., & Pinheiro, L. (2009). Water column seismic images as maps of temperature gradient. *Oceanography*, *22*(1), 192–205.

Ruddick, B. R. (2018). Seismic oceanography's failure to flourish: A possible solution. *Journal of Geophysical Research: Oceans*, *123*(1), 4–7. doi: 10.1002/2017JC013736

Rudnick, D. L., & Cole, S. T. (2011). On sampling the ocean using underwater gliders. *Journal of Geophysical Research: Oceans*, *116*(C8). doi: 10.1029/2010JC006849

Sallarès, V., Biescas, B., Buffett, G., Carbonell, R., Dañobeitia, J. J., & Pelegrí, J. L. (2009). Relative contribution of temperature and salinity to ocean acoustic reflectivity. *Geophysical Research Letters*, *36*(24). (L00D06) doi: 10.1029/2009GL040187

Sheen, K. L., White, N., Caulfield, C. P., & Hobbs, R. W. (2011). Estimating Geostrophic Shear from Seismic Images of Oceanic Structure. *Journal of Atmospheric and Oceanic Technology*, *28*(9), 1149–1154. doi: 10.1175/JTECH-D-10-05012.1

Sheen, K. L., White, N. J., & Hobbs, R. W. (2009). Estimating mixing rates from seismic images of oceanic structure. *Geophysical Research Letters*, *36*(24). (L00D04) doi: 10.1029/2009GL040106

Shelton, R., Turrell, W., Macdonald, A., McLaren, I., & Nicoll, N. (1997). Records of post-smolt Atlantic salmon, *Salmo salar* L., in the Faroe-

©2020 American Geophysical Union. All rights reserved.

Shetland Channel in June 1996. *Fisheries Research*, *31*(1-2), 159–162. doi: 10.1016/S0165-7836(97)00014-3

Sheriff, R. E., & Geldart, L. P. (1995). *Exploration Seismology*. Cambridge University Press.

Sherwin, T. (1991). Evidence of a deep internal tide in the Faeroe-Shetland Channel. *Tidal Hydrodynamics*, 469–488.

Sherwin, T. J. (1995). Tidal oscillations of the thermocline in the Faroe-Shetland Channel. *Ocean Challenge*, *6*, 33–35.

Sherwin, T. J., Turrell, W. R., Jeans, D. R. G., & Dye, S. (1999). Eddies and a mesoscale deflection of the slope current in the Faroe-Shetland Channel. *Deep Sea Research Part I: Oceanographic Research Papers*, *46*(3), 415–438. doi: 10.1016/S0967-0637(98)00077-6

Sherwin, T. J., Williams, M. O., Turrell, W. R., Hughes, S. L., & Miller, P. I. (2006). A description and analysis of mesoscale variability in the Färoe-Shetland Channel. *Journal of Geophysical Research: Oceans*, *111*(C3). doi: 10.1029/2005JC002867

Simpson, J., Dickey, T., & Koblinsky, C. (1984). An offshore eddy in the California current system Part I: Interior dynamics. *Progress in Oceanography*, *13*(1), 5–49. doi: 10.1016/0079-6611(84)90004-1

Song, H., Pinheiro, L. M., Ruddick, B., & Huang, X. (2012). Seismic oceanography: A new geophysical tool to investigate the thermohaline structure of the oceans. *Oceanography*, 113–128.

Sreenivasan, K. R. (1996). The passive scalar spectrum and the Obukhov-Corrsin constant. *Physics of Fluids*, *8*(1), 189–196. doi: doi.org/10.1063/1.868826

Stammer, D., & Wunsch, C. (1994). Preliminary assessment of the accuracy and precision of TOPEX/POSEIDON altimeter data with respect to the large-scale ocean circulation. *Journal of Geophysical Research: Oceans*, *99*(C12), 24584–24604. doi: 10.1029/94JC00919

Swallow, J., Gould, W., & Saunders, P. (1977). Evidence for a poleward eastern boundary current in the North Atlantic Ocean. *ICES CM*, *100*, 32.

Tang, Q., Gulick, S., & Sun, L. (2014). Seismic observations from a Yakutat eddy in the northern Gulf of Alaska. *Journal of Geophysical Research: Oceans*, *119*(6), 3535–3547. doi: 10.1002/2014JC009938

©2020 American Geophysical Union. All rights reserved.

Tang, Q., Gulick, S. P. S., Sun, J., Sun, L., & Jing, Z. (2019). Submesoscale features and turbulent mixing of an oblique anticyclonic eddy in the Gulf of Alaska investigated by marine seismic survey data. *Journal of Geophysical Research: Oceans*, *125*(1), e2019JC015393. doi: 10.1029/2019JC015393

Tang, Q., Tong, V. C. H., Hobbs, R. W., & Maqueda, M. Á. M. (2019). Detecting changes at the leading edge of an interface between oceanic water layers. *Nature Communications*, *10*(1), 1–8. doi: 10.1038/s41467-019-12621-8

Turrell, W. R., Hansen, B., Hughes, S., & Østerhus, S. (2003). Hydrographic variability during the decade of the 1990s in the Northeast Atlantic and southern Norwegian Sea. In *ICES Marine Science Symposia* (Vol. 219, pp. 111–120).

Turrell, W. R., Slesser, G., Adams, R. D., Payne, R., & Gillibrand, P. A. (1999). Decadal variability in the composition of Faroe Shetland Channel bottom water. *Deep Sea Research Part I: Oceanographic Research Papers*, *46*(1), 1–25. doi: 10.1016/S0967-0637(98)00067-3

Ullgren, J. E., Fer, I., Darelius, E., & Beaird, N. (2014). Interaction of the Faroe Bank Channel overflow with Iceland Basin intermediate waters. *Journal of Geophysical Research: Oceans*, *119*(1), 228–240. doi: 10.1002/2013JC009437

Vsemirnova, E., Hobbs, R., Serra, N., Klaeschen, D., & Quentel, E. (2009). Estimating internal wave spectra using constrained models of the dynamic ocean. *Geophysical Research Letters*, *36*(24). doi: 10.1029/2009GL039598

Vsemirnova, E. A., Hobbs, R. W., & Hosegood, P. (2012). Mapping turbidity layers using seismic oceanography methods. *Ocean Science*, *8*(1), 11–18. doi: 10.5194/os-8-11-2012

Wang, Y. (2015). Frequencies of the Ricker wavelet. *Geophysics*, *80*(2), A31–A37. doi: 10.1190/geo2014-0441.1

Welch, P. (1967). The use of fast Fourier transform for the estimation of power spectra: A method based on time averaging over short, modified periodograms. *IEEE Transactions on Audio and Electroacoustics*, *15*(2), 70–73. doi: 10.1109/TAU.1967.1161901

Wunsch, C. (1997). The vertical partition of oceanic horizontal kinetic energy. *Journal of Physical Oceanography*, *27*(8), 1770–1794. doi: 10.1175/1520-0485(1997)027⟨1770:TVPOOH⟩2.0.CO;2

Wunsch, C., & Ferrari, R. (2004). Vertical mixing, energy, and the general circula-

©2020 American Geophysical Union. All rights reserved.

tion of the oceans. *Annual Review of Fluid Mechanics*, *36*, 281–314. doi: 10.1146/annurev.fluid.36.050802.122121

Yale, M. M., Sandwell, D. T., & Smith, W. H. (1995). Comparison of along-track resolution of stacked Geosat, ERS 1, and TOPEX satellite altimeters. *Journal of Geophysical Research: Solid Earth*, *100*(B8), 15117–15127. doi: 10.1029/95JB01308

Yamazaki, H., & Lueck, R. (1990). Why oceanic dissipation rates are not lognormal. *Journal of Physical Oceanography*, *20*(12), 1907–1918. doi: 10.1175/1520-0485(1990)020⟨1907:WODRAN⟩2.0.CO;2

Yang, Q., Zhao, W., Liang, X., Dong, J., & Tian, J. (2017). Elevated mixing in the periphery of mesoscale eddies in the South China Sea. *Journal of Physical Oceanography*, *47*(4), 895–907. doi: 10.1175/JPO-D-16-0256.1

Yilmaz, Ö. (2001). *Seismic Data Analysis: Processing, Inversion, and Interpretation of Seismic Data*. Society of Exploration Geophysicists. doi: 10.1190/1.9781560801580

Accepted Article

©2020 American Geophysical Union. All rights reserved.

1156 **A Seismic Acquisition Details**

Accepted Article

©2020 American Geophysical Union. All rights reserved.

Accepted Article

Table A.1. Details of individual transects.

Transect	Compass bearing / °	Start date	Start time	End date	End time	Length / km	Mean vessel speed / m s^{-1}
A1	047	208	01:39	208	02:48	8.7	2.10 ± 0.15
B1	227	208	05:41	208	06:35	7.4	2.28 ± 0.15
A2	047	208	20:53	208	22:10	8.7	1.88 ± 0.12
B2	227	209	01:36	209	02:38	7.4	1.99 ± 0.12
A3	047	209	17:23	209	18:30	8.6	2.14 ± 0.15
B3	227	210	03:56	210	04:54	7.3	2.10 ± 0.14
A4	047	210	19:21	210	20:26	8.6	2.21 ± 0.14
B4	227	210	23:27	211	00:23	7.1	2.11 ± 0.13
A5	047	214	14:56	214	15:59	8.7	2.30 ± 0.16
B5	227	214	18:58	214	19:57	7.1	2.01 ± 0.13
A6	047	215	10:50	215	11:56	8.6	2.17 ± 0.15
B6	227	215	15:17	215	16:10	7.0	2.20 ± 0.14
A7	047	216	06:48	216	07:52	8.7	2.27 ± 0.15
B7	227	216	11:07	216	12:08	7.1	1.94 ± 0.12
A8	047	217	02:00	217	03:08	8.7	2.13 ± 0.14
B8	227	217	06:17	217	07:09	7.0	2.24 ± 0.15
A9	047	217	20:40	217	21:43	8.7	2.30 ± 0.15
B9	227	218	00:34	218	01:33	6.9	1.95 ± 0.13

manuscript submitted to *JGR: Oceans*

©2020 American Geophysical Union. All rights reserved.

Accepted Article

Table A.2. Table A.1 continued.

Transect	Compass bearing / °	Start date	Start time	End date	End time	Length / km	Vessel speed / m s^{-1}
A10	047	218	15:45	218	16:53	8.6	2.11 ± 0.16
B10	227	218	19:43	218	20:40	6.8	1.99 ± 0.14
A11	047	219	10:29	219	11:32	8.6	2.28 ± 0.16
B11	227	219	14:25	219	15:21	6.8	2.02 ± 0.14
A12	047	220	04:58	220	06:00	8.6	2.31 ± 0.15
B12	227	220	09:01	220	10:00	6.7	1.89 ± 0.13
A13	047	221	08:54	221	09:51	8.6	2.51 ± 0.16
B13	227	221	12:52	221	13:50	6.7	1.93 ± 0.13
A14	047	222	01:27	222	02:25	8.6	2.47 ± 0.16
B14	227	222	05:07	222	05:56	6.6	2.24 ± 0.15
A15	047	222	17:38	222	18:42	8.6	2.24 ± 0.13
B15	227	222	21:31	222	22:25	6.5	2.01 ± 0.16
A16	047	223	17:25	223	18:24	8.6	2.43 ± 0.18
B16	227	223	21:03	223	21:51	6.6	2.29 ± 0.16
A17	227	224	08:12	224	09:12	8.6	2.39 ± 0.16
B17	227	224	11:51	224	12:39	6.6	2.29 ± 0.15
A18	047	225	00:05	225	01:03	8.6	2.47 ± 0.14
B18	227	225	03:38	225	04:28	6.6	2.20 ± 0.16

manuscript submitted to *JGR: Oceans*

©2020 American Geophysical Union. All rights reserved.

Accepted Article

Table A.3. Table A.1 continued.

Transect	Compass bearing / °	Start date	Start time	End date	End time	Length / km	Vessel speed / m s^{-1}
A19	047	225	15:38	225	16:37	8.6	2.43 ± 0.16
B19	227	225	19:12	225	20:00	6.6	2.29 ± 0.17
A20	047	226	06:42	226	07:46	8.6	2.24 ± 0.16
B20	227	226	10:20	226	11:09	6.6	2.24 ± 0.16
A21	047	226	21:53	226	22:59	8.6	2.17 ± 0.15
B21	227	227	01:37	227	02:29	6.6	2.12 ± 0.15
A22	047	227	13:51	227	15:01	8.7	2.07 ± 0.15
B22	227	227	17:58	227	18:51	6.5	2.04 ± 0.14
A23	047	228	06:00	228	07:02	8.7	2.34 ± 0.16
B23	227	228	09:52	228	10:53	6.6	1.80 ± 0.12
A24	047	228	22:01	228	23:02	8.7	2.38 ± 0.16
B24	227	229	01:44	229	02:41	6.6	1.93 ± 0.14
A25	047	229	17:02	229	18:00	8.6	2.47 ± 0.18
B25	227	229	20:59	229	21:59	6.6	1.83 ± 0.15
A26	047	230	08:12	230	09:11	8.6	2.43 ± 0.16
B26	227	230	12:12	230	13:04	6.5	2.08 ± 0.14
A27	047	230	23:13	231	00:17	8.7	2.27 ± 0.14
B27	047	232	04:00	232	04:55	7.8	2.36 ± 0.15

manuscript submitted to *JGR: Oceans*

©2020 American Geophysical Union. All rights reserved.

B Reflective Tilt

B.1 Effect of Current on Imaged Tilting

The influence of advection along the channel axis on the tilt of imaged fine-scale structure is investigated using a simple model, in which the effects of repeated cmp sampling are ignored. Thermohaline structure is advected with an in-plane component of current velocity that is denoted by u_c. This structure is imaged by a vessel moving at speed u_v. In a time t, the vessel travels a distance $x = u_v t$ across the sea surface. Over this distance, the vessel images advected fine-scale structure that has a total length of $x_f = (u_v - u_c)t$. The imaged fine-scale structure has an actual gradient, $\tan(\gamma_f)$, that is given by

$$\tan(\gamma_f) = \frac{\Delta z}{x_f}, \tag{B.1}$$

where Δz is change in depth across a horizontal distance, x_f. $\tan(\gamma)$ estimated from the seismic image is given by

$$\tan(\gamma) = \frac{\Delta z}{x} = \left(1 - \frac{u_c}{u_v}\right)\tan(\gamma_f). \tag{B.2}$$

If thermohaline structure is advected in the same direction as vessel motion (i.e. $\frac{u_c}{u_v} > 0$), reflective gradients will be underestimated. If thermohaline structure is advected in the opposite direction to vessel motion (i.e. $\frac{u_c}{u_v} < 0$), reflective gradients are overestimated. Taking extremal values of $u_c = 1$ m s^{-1} and $u_v = 2$ m s^{-1}, $\tan(\gamma) = 0.5\tan(\gamma_f)$ for $\frac{u_c}{u_v} > 0$ and $\tan(\gamma) = 1.5\tan(\gamma_f)$ for $\frac{u_c}{u_v} < 0$.

B.2 Rossby Radius of Deformation

The value of L_R is estimated by approximating the density structure of water within the Faroe-Shetland Channel using a two-layer model (e.g. Gerkema, 1996). Upper and lower layers have depths of H_1 and H_2 and densities of ρ_1 and ρ_2, respectively. L_R is given by

$$L_R = \frac{\sqrt{g'H}}{f}, \tag{B.3}$$

where $H \approx H_1 \approx H_2$ and f is the Coriolis parameter. g' is reduced gravity, which is given by

$$g' = \frac{g\Delta\rho}{\rho}, \tag{B.4}$$

©2020 American Geophysical Union. All rights reserved.

where g is gravitational acceleration, $\Delta\rho = (\rho_2 - \rho_1)$ is density contrast between the two layers, and $\rho = \rho_2 \approx \rho_1$. Taking $H \approx 500$ m, $\Delta\rho \approx \langle\Delta\rho_\theta\rangle_p = 0.6$ kg m^{-3}, $\rho \approx \bar{\rho}_{\theta_1} = 1027.6$ kg m^{-3} and $f \approx 1.29 \times 10^{-4}$ s^{-1} yields $L_R \approx 13$ km.

B.3 Estimation of Geostrophic Shear

Assuming geostrophic balance, the change in the out-of-plane (i.e. northwest-southeast) component of geostrophic velocity across the pycnocline, $(\Delta U_p)_\perp$, can be estimated from a single seismic image using

$$(\Delta U_p)_\perp = \frac{g}{f} \frac{\langle\mu\rangle_p \langle\Delta\rho_\theta\rangle_p}{\langle\rho_\theta\rangle_p} \langle\tan(\gamma)\rangle_p , \tag{B.5}$$

where $\perp$ indicates the out-of-plane component (Sheen et al., 2011; Tang et al., 2014) and μ is the ratio of the fractional change in *in situ* density to the fractional change in potential density across an interface (Sheen et al., 2011; Tang et al., 2014). We estimate a pycnoclinic value of $\langle\mu\rangle_p = 1.2 \pm 0.2$ from CTD profiles following the method described by McDougall (1988).

Estimated values of $(\Delta U_p)_\perp$ lie within the range of -0.7 to 1.0 m s^{-1} (Figure 7). Corresponding magnitudes of out-of-plane shear across the pycnocline are $\lesssim 4\times10^{-3}$ s^{-1}. Numerical uncertainties for values of $(\Delta U_p)_\perp$ are estimated by combining errors associated with $\langle\mu\rangle_p$, $\langle\Delta\rho_\theta\rangle_p$, $\langle\rho_\theta\rangle_p$ and $\langle\tan(\gamma)\rangle_p$ in quadrature. Cumulative uncertainties are smaller than ±0.5 m s^{-1}. Note that these uncertainties do not address the validity of a geostrophic approximation. Estimates of $(\Delta U_p)_\perp$ are limited to the pycnocline since reflections are visible only at these depths. Absolute geostrophic velocities cannot be estimated since there is no reliable level of known motion.

C Estimations of Diapycnal Diffusivity

C.1 Noise Suppression

We minimize the effect of ambient and harmonic noise on horizontal spectra computed from seismic images by following the approach of Holbrook et al. (2013). Spectral content is determined by using signal-to-noise ratios and direct data transforms. To identify frequency bands that are least affected by white noise, we applied a trapezoidal band-pass frequency filter with a central width of 10 Hz (e.g. corner frequencies of 10–20–30–40 Hz) to seismic records before stacking. Turbulent subranges were most clearly

©2020 American Geophysical Union. All rights reserved.

imaged for the frequency range $\sim$ 30–80 Hz, for which signal-to-noise ratios > 4 were found. Signal at frequencies > 80 Hz contained little power and therefore no filtering aside than application of the initial low-cut ($<$ 30 Hz) Butterworth filter was carried out. Use of different frequency filters does not significantly affect the results.

This strategy acts to suppress the effects of ambient noise as far as possible. However, some direct data transforms contain spikes caused by harmonic noise (Holbrook et al., 2013). This form of noise is caused by periodic variations in the length of acoustic ray paths between cmps. Holbrook et al. (2013) use a notch filter to remove sharply defined spikes. Here, we do not apply a notch filter since we found that harmonic noise does not adversely affect reflections that are deeper than $\gtrsim 300$ m.

C.2 Frequency-Wavenumber Smearing

Horizontal wavenumber spectra are computed from seismic images under the assumption that fine-scale structure is stationary over the time taken to image an individual tracked reflection. If fine-scale structure is not stationary, finite sampling speed will smear variability in frequency space into variability in horizontal wavenumber space (Klaeschen et al., 2009). Energy at wavenumber k_x is smeared to a new wavenumber, k_x', which is given by

$$k_x' = k_x - \frac{f_s}{u_v}, \tag{C.1}$$

where f_s is the frequency of oscillation of imaged structure and u_v is vessel speed in the direction of propagation of fine-scale structure (Rudnick & Cole, 2011; E. Vsemirnova, Hobbs, Serra, Klaeschen, & Quentel, 2009). The effects of repeated cmp sampling are ignored. If the vessel moves in the same direction as the current but at a higher speed, power is shifted to lower wavenumbers (Garrett & Munk, 1972). If the vessel travels against the current, power is shifted to higher wavenumbers. Taking the most extreme but still physically reasonable value of $f_s = 6$ cph and the observed range of $1.8 \lesssim u_v \lesssim 2.5$ m s^{-1}, the maximum magnitude of these shifts is estimated to be $\sim 9{\times}10^{-4}$ cpm. Turbulent motions at wavenumbers greater than 10^{-2} cpm are insignificantly affected.

C.3 Identification of Turbulent Spectral Subranges

We identify turbulent subranges in mean spectra of the horizontal gradient of vertical displacement, $\langle \phi_{\xi_x} \rangle_p$, by fitting a model spectrum. This model comprises, in order

©2020 American Geophysical Union. All rights reserved.

Accepted Article

of increasing horizontal wavenumber, a low-wavenumber subrange of variable gradient, a turbulent subrange of gradient +1/3, and a white noise subrange of gradient +2. Four parameters control the exact form of the model: the gradient, a, of the low-wavenumber subrange; the co-ordinates, (b, c), of the intersection point between the low-wavenumber and turbulent regimes; and the width, d, of the turbulent subrange. The model is fitted by defining a misfit function

$$M_{A1} = \sum_{i=1}^{D} \left[\left[\log_{10}(\phi_{\xi_x}^m) \right]_i - \left[\log_{10}(\langle \phi_{\xi_x} \rangle_p) \right]_i \right]^2, \tag{C.2}$$

where $\phi_{\xi_x}^m$ is the model and D is the number of points in the power spectrum. Best-fitting values of a, b, c and d are found by minimizing M_{A1} using Powell's conjugate direction algorithm (M. J. D. Powell, 1964). We note that fitting a model of this form implicitly assumes a sharp transition between the low-wavenumber (i.e. internal wave) and turbulent spectral subranges. The exact nature of this transition is uncertain and it is possible that internal waves and turbulence co-exist at intermediate scales (D'Asaro & Lien, 2000; Falder et al., 2016; Klymak & Moum, 2007a, 2007b). Nevertheless, at sufficiently high wavenumbers away from the transition, it is straightforward to identify spectral subranges that clearly belong to the turbulent regime.

C.4 Error Analysis

Numerical uncertainties in estimated values of K depend on uncertainties in $\hat{c}$, $\langle N \rangle_p$, Γ and C_T. Error in the fitted intercept of a straight line of fixed gradient is given by

$$\sigma_{\hat{c}} = \sqrt{\frac{1}{\sum_{i=1}^{D} \frac{1}{\sigma_i^2}}}, \tag{C.3}$$

where $\sigma_{\hat{c}}$ is the error on $\hat{c}$, σ_i is the standard deviation on the i^{th} point of the mean spectrum $\langle \phi_{\xi_x} \rangle_p$, and D is the total number of points in the mean spectrum. Estimated $\sigma_{\hat{c}}$ are in the range 0.017–0.1. Errors in $\hat{c}$ and $\langle N \rangle_p$ are combined in quadrature to yield

$$(\sigma_K)^2 = \left(\frac{3}{2} \sigma_{\hat{c}} \right)^2 + \left(\log_{10}(e) \frac{\sigma \langle N \rangle_p}{\langle N \rangle_p} \right)^2, \tag{C.4}$$

where σ_K and $\sigma \langle N \rangle_p$ are the uncertainties in $\log_{10}(K)$ and $\langle N \rangle_p$, respectively, and it has been assumed that $\sigma_{\hat{c}}$ and $\sigma \langle N \rangle_p$ are normally distributed. For $\sigma_{\hat{c}}$ in the range 0.017–0.1 and $\langle N \rangle_p = 2.0 \pm 0.3$ cph, errors on $\log_{10}(K)$ are in the range $\sim$ 0.07–0.17 logarithmic units. If, instead of the value of $\langle N \rangle_p = 2.0 \pm 0.3$ cph estimated from CTD casts, a value of $\langle N \rangle_p = 2 \pm 1$ cph is used, uncertainties in $\log_{10}(K)$ are in the range $\sim$ 0.22–0.26 logarithmic units.

©2020 American Geophysical Union. All rights reserved.

In assessing the the effect of uncertainties in Γ and C_T, we do not formally propagate errors because the underlying probability distributions are not accurately determined. Instead, the effects of choosing the lower and upper bounds given by Sreenivasan (1996) and Mashayek et al. (n.d.) are explored. Taking lower and upper bounds of $\Gamma = 0.1$ and $\Gamma = 0.4$, respectively, implies that assumption of a constant value of $\Gamma = 0.2$ introduces an uncertainty in $\log_{10}(K)$ of $\lesssim 0.15$ logarithmic units as shown by

$$\log_{10}(K) = -\frac{1}{2}\log_{10}(\Gamma) + A \tag{C.5}$$

$$= (0.5 + A) \text{ logarithmic units for } \Gamma = 0.1 \tag{C.6}$$

$$\approx (0.35 + A) \text{ logarithmic units for } \Gamma = 0.2 \tag{C.7}$$

$$\approx (0.2 + A) \text{ logarithmic units for } \Gamma = 0.4, \tag{C.8}$$

where A includes all terms that are independent of Γ. A similar analysis shows that, for C_T in the range 0.3–0.5, assumption of constant $C_T = 0.4$ introduces uncertainties in $\log_{10}(K)$ of up to 0.1 logarithmic units.

Accepted Article

©2020 American Geophysical Union. All rights reserved.